Suppression of Thermoacoustic Instabilities in a Swirl Combustor through Microjet Air Injection

by

Zachary Alexander LaBry

Submitted to the Department of Mechanical Engineering
in partial fulfillment of the requirements for the degree of

Masters of Science in Mechanical Engineering

at the

MASSACHUSETTS INSTITUTE OF TECHNOLOGY

June 2010

Author .....
Department of Mechanical Engineering
May 19, 2010

Certified by .....
Ahmed F. Ghoniem
Ronald C. Crane ('72) Professor
Thesis Supervisor

Accepted by .....
David E. Hardt
Chairman, Department Committee on Graduate Theses

Suppression of Thermoacoustic Instabilities in a Swirl Combustor through Microjet Air Injection

by

Zachary Alexander LaBry

Submitted to the Department of Mechanical Engineering
on May 19, 2010, in partial fulfillment of the
requirements for the degree of
Masters of Science in Mechanical Engineering

Abstract

Thermoacoustic or combustion instability, a positive feedback loop coupling heat release rate and acoustic oscillations in a combustor, is one of the greatest challenges currently facing the development of new gas turbine systems for propulsion and power generation. Traditional gas turbine designs have bypassed the problem of combustion instability by designing non-premixed combustors around a fixed operating point. Increasing trends toward lower emissions and greater fuel flexibility have placed more emphasis on developing lean-premixed combustors that are stable over a range of operating conditions.

This thesis explores two aspects of combustion instability in the context of a swirl-stabilized, lean-premixed combustor: the role of the major coherent flow structures, and the potential for using secondary air injection to passively suppress combustion instability. Microjets inject air into the combustion chamber in the flame anchoring zone. These microjet injectors attempt to modify the flow field so as to break the feedback mechanism between the chamber acoustics and the heat release rate. Eight microjet injector configurations are studied. Flow is injected axially into the outer recirculation zone or radially into the inner recirculation zone. The injectors inject air with either no swirl, the same swirl direction as the main air flow, or the opposite swirl direction as the main air flow. Chamber acoustics are measured using sensitive microphones. The flame and flow field are interrogated using high-speed imaging and stereoscopic particle image velocimetry.

The bulk of this work was conducted for lean propane/air flames, slightly above the lean blowoff limit. Two modes of instability were examined: the 1/4 wave mode at 40 Hz, and the 3/4 wave mode at 105 Hz. Without microjet injection, the combustor transitions directly from the 1/4 wave mode instability to the 3/4 wave mode instability as the equivalence ratio is increased above 0.58. Counter-swirling radial microjets injecting air into the inner recirculation zone increased the lower limit of the 3/4 wave mode to an equivalence ratio of 0.62 and reduced the amplitude of the 1/4 wave mode, effectively creating a stable operating regime for equivalence ratios between the two modes. Microjet injector tests indicate that the inner recirculation

zone has a dominant role in the dynamic stabilization of the flame. This observation is confirmed by stereoscopic PIV measurements that reveal periodic formation and collapse of the vortex breakdown bubble in the 3/4 wave mode and vortex shedding in the inner recirculation zone in the 1/4 wave mode.

Thesis Supervisor: Ahmed F. Ghoniem
Title: Ronald C. Crane ('72) Professor

Acknowledgments

I would like to thank my advisor, Professor Ahmed Ghoniem, for giving me the opportunity to conduct this reseach in the Reacting Gas Dynamics Laboratory and allowing me the freedom to choose and develop the direction that this research has taken.

I also owe a great deal of gratitude to my colleagues in the RGD. Dr. Ray Speth has contributed substantially to my knowledge of combustion dynamics and my development as a researcher. His ability to diagnose and debug any problem with any piece of hardware or software has enabled much of this research to be completed in the time that it has. I would also like to thank Dr. Santosh Shanbhogue, who brought with him expertise in both combustion and optical diagnostics, and an enthusiasm for experimental work that made long hours of collecting data

This work was funded by the King Abdullah University of Science and Technology grant number KUA-110-010-01 and the United States Department of Energy grant number SUB 05-21-SR121 through the University Turbine Systems Research Program.

Contents

List of Figures

Chapter 1

Introduction

Increasing emphasis on the development of low emission technologies for gas turbines has placed great demand on the search for technologies with low emissions and high power-density. Although many new technologies are emerging with an emphasis on low emissions, continuous combustion systems often remain the most viable solutions for high power-density applications such as power generation and aircraft propulsion. Among the concepts for reducing combustion emissions, lean-premixed (LPM) and lean-premixed-prevaporized (LPP) combustion (for gaseous and liquid fuels, respectively) are among the most promising, particulary for reducing thermal nitric oxide (NO, NO_2, N_2O and others, collectively known as NO_x) emissions.

Reduction of NO_x emissions has been the subject of a significant amount of research due to the wide-ranging adverse effects that these pollutants can have on health and the environment. The environmental impacts from NO_x emissions range from the production of acid rain to the reduction of stratospheric ozone and the creation of tropospheric ozone. As a result, NO_x emissions have been the subject of previous legislation, such as the Clean Air Act in the United States, and of current and future legislative efforts.

The primary mechanism of NO_x emission in fuel-lean combustion is the reaction of O atoms with N_2 molecules ("thermal NO_x" emissions). This pathway for NO_x production is sensitive to temperatures near those encountered in hydrocarbon flames, and large emission reductions can be achieved by lowering the maximum flame

temperature. As combustion products must be cooled as they leave the combustion chamber in order to meet structural limits, this reduction in emissions can, in principle, be achieved without a reduction in overall system efficiency (see Beér [4]).

Traditional gas turbines operate in a non-premixed mode. Even though the overall mixture may be fuel-lean, flame temperatures may be high for these combustors. In a lean-premixed combustor, fuel and air are thoroughly mixed at lean equivalence ratios prior to entering the combustion chamber, to avoid creating locally rich mixtures and high local flame temperatures.

The major drawback limiting LPM technology is combustion instability. Damping mechanisms that are present in non-premixed flames are not present in premixed combustion, and LPM combustors can enter dynamically unstable modes of operation in which oscillations in the heat release rate, chamber acoustics and fluid dynamics couple. These high-amplitude oscillations can lead to structural damage, unacceptable levels of noise pollution, flame flashback, and blowoff.

At present, the physics that lead to combustion instability are not sufficiently well understood to be able to predict the onset of instability in the design phase. Costly experimentation is necessary in order to develop premixed combustion systems, and compromises in emission production are often necessary.

Practical combustor geometries are often complex, balancing combustion, heat transfer, and fluid mechanic design properties with cost, weight, and structural considerations. In this thesis, the subject of investigation is an idealized combustor, employing an axisymmetric combustion chamber with an sudden increase in area in the combustion chamber downstream of a swirler. As many commercial combustors employ sudden expansions and swirl for fuel/air mixing and flame anchoring, this laboratory scale combustor is intended to mimic some of the basic physics that are significant in practical combustors.

The problem of combustion instability in lean-premixed combustion presents both an interesting scientific problem as well as an important technological challenge to be overcome. The purpose of this thesis is two-fold: to present work that has been done to provide insight into the interplay between combustion instability and the

dominant flow structures in a swirl-stabilized combustor, and to investigate the use of secondary air injection for mitigating instabilities.

1.1 Thermoacoustic Instability

In general terms, *thermoacoustic instability* is the coupling between the chamber acoustic and the heat release rate in a combustion system that leads to self-sustaining, high-amplitude, discrete oscillations. Depending on the geometry, these instabilities may be tied to different modes of the combustor. Longitudinal modes that are bounded by the inlet and outlet of the combustor, as well as transverse modes with periodic boundaries are both commonly observed. More complex geometries can lead to a greater diversity of modes, and more opportunity for instability.

In order for thermoacoustic instabilities to exist, harmonic oscillations between heat release and acoustic pressure must interact constructively. Rayleigh first observed that these two processes must be in phase for the heat release oscillations to constructively add energy to the acoustic oscillations.

> If heat be periodically communicated to, and abstracted from, a mass of air vibrating (for example) in a cylinder bounded by a piston, the effect produced will depend upon the phase of the vibration at which the transfer of heat takes place. If heat be given to the air at the moment of greatest condensation, or taken from it at the moment of greatest rarefaction, the vibration in encouraged. On the other hand, if heat be given at the moment of greatest rarefaction, or abstracted at the moment of greatest condensation, the vibration is discouraged. [5]

Rayleigh's qualitative observations were grounded on stronger theoretical and mathematical principles in by the work of Chu [6] and others. We define the Rayleigh index, $\mathcal{R}$, as

$$\mathcal{R} \equiv \int_{\tau} \int_{\Omega} p' q' d\Omega dt \tag{1.1}$$

where p' and q' are the pressure and heat release fluctuations, respectively, in the volume Ω integrated over τ, the time for one cycle of the oscillation. Rayleigh's

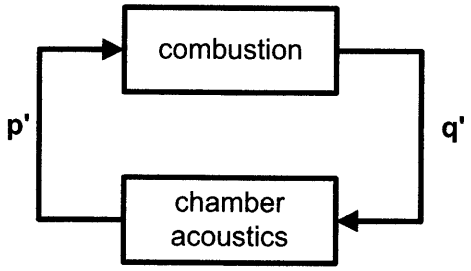

Figure 1-1: Positive feedback loop between chamber acoustics and heat release.

criterion is expressed by stating that $\mathcal{R} > 0$ implies that oscillations will grow, while $\mathcal{R} < 0$ implies that oscillations will decay.

Although $\mathcal{R} > 0$ is a necessary condition for the presence of thermoacoustic instability, it is not a predictive tool and does not provide physical insight into the mechanisms of instability. Fundamentally, dynamic combustion instability is the result of a positive feedback loop that couples the chamber acoustics and heat release as sketched in Fig. 1-1. When appropriately perturbed, fluctuations are able to positively reinforce themselves, eventually leading to the pressure and heat release reaching a limit cycle. Only a small fraction of the energy released in the combustion process is necessary to drive acoustic oscillations, and this energy is transfered via turbulent and period fluid stresses [7].

Heat release oscillations can couple with other dynamical aspects of the combustion process, reinforcing thermoacoustic instability. Two examples are equivalence ratio oscillations and flame-wall interactions. Equivalence ratio oscillations can couple with the acoustics if pressure waves are permitted to travel upstream of where the fuel injection occurs. Downstream heat release oscillations will lag behind equivalence ratio oscillations due to the time necessary for the flow to convect into the combustion chamber. Although important, this experiment was designed to isolate the fuel injection and mixing process from the chamber acoustics by placing the injectors upstream of a choke plate, and so this effect is not explored in detail.

Heat transfer through the wall reduces the consumption speed of the flame near the wall. If local velocity exceeds the flame propagation velocity, then the flame will move away from the wall. Heat loss to the wall will decrease, and the flame speed will

increase. This heat release oscillation is also a potential mechanism for reinforcing thermoacoustic instability.

1.2 Vortex Breakdown in Swirling Flows

Swirling flows are commonly used in gas turbines to aid in fuel/air mixing and for flame anchoring. In strongly swirling flows, longitudinal vorticity becomes unstable and vortex lines tilt and stretch forming annular vortices. Annular vortices create a recirculation zone that acts to circulate hot combustion products upstream to ignite the incoming reactants, and prevents the flame from being convected downstream. This region of local recirculation is known as a *vortex breakdown.*

Although vortex breakdown can take on many distinct, asymmetric forms, the most common mode of vortex breakdown in a strongly swirling flow is the axisymmetric bubble-type vortex breakdown. The concept swirl is quantified by means of a dimensionless parameter known as the swirl number (S), which is defined as the ratio of the axial flux of tangential momentum to the axial flux of axial momentum times the inlet radius (see [8]).

For an axisymmetric, confined flow with an inlet radius of R_0 and a maximum radius of R, the swirl number can be expressed as

$$S \equiv \frac{G_\theta}{G_z R_0} \tag{1.2}$$

where the flux of tangential momentum G_θ is given by

$$G_\theta \equiv 2\pi \int_0^R \rho u_z u_\theta r^2 dr \tag{1.3}$$

and the flux of axial momentum is given by

$$G_z \equiv 2\pi \int_0^R \rho u_z^2 r dr \tag{1.4}$$

The quantities u_z, u_θ, and ρ are the axial velocity, tangential velocity, and density,

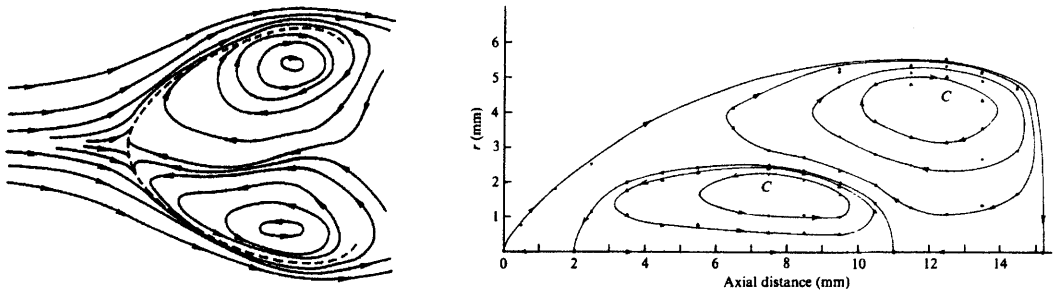

(a) (b)

Figure 1-2: Experimentally measured internal structure of a two-cell bubble-type vortex breakdown (**a**) [1] and (b) a four-cell bubble-type vortex breakdown (**b**) [2].

respectively.

Different variants of the bubble-type vortex breakdown have been observed: the two-celled bubble (Fig. 1-2(a)), and the four celled bubble (Fig. 1-2(b)), which is observed at higher swirl numbers. Faler and Leibovich [2] experimentally investigated the four-cell bubble-type breakdown, concluding that while the bubble was visually axisymmetric, the internal structure showed time-dependence and azimuthal asymmetries. Numerical simulations based on the solution of the full, time-dependent, three-dimensional Navier Stokes equations by Spall, *et. al.* [9] confirmed these time-dependent nature and azimuthal assymmetries, noting that the vortex centers fluctuate with time.

Wang and Rusak [10] developed a theoretical framework for bubble-type vortex breakdown in a pipe, working from a prior theoretical model propose by Benjamin [11], which treated the vortex breakdown as a transitional state between supercritical and subcritical flows. The model was based on a weakly non-linear perturbation of the Euler equation (the Squire-Long equation), and showed that columnar flow is always a stable, but above a certain level of swirl, a vortex breakdown mode is also stable. For very high swirl, the vortex breakdown mode joins the columnar solution.

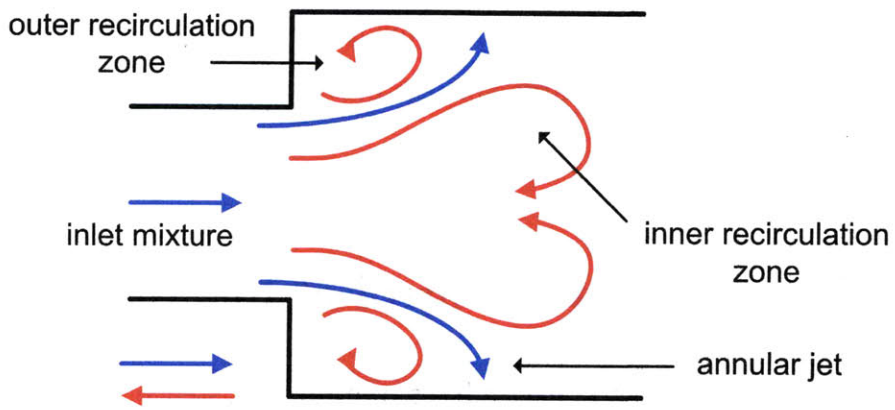

Figure 1-3: Flowfield schematic in the flame anchoring region of a swirl-stabilized combustor with a sudden expansion showing the inner recirculation zone, outer recirculation zone, and annular jet.

1.3 Flame-Vortex Interaction

There are three dominant flow features inside the combustion chamber of swirl-stabiized combustor with a sudden area expansion, which are shown in Fig. 1.3: the inner recirculation zone and the outer recirculation zone, separated by an annular jet. The inner recirculation zone (sometimes known as the central recirculation zone) is a region of reversed flow created through the mechanism of vortex breakdown, as discussed in §1.2. The outer recirculation zone (sometimes known as the corner recirculation zone) is an annular region of separated flow at the outermost upstream position in the expanded combustion chamber. Between these two recirculation zones, an annular jet feeds fresh reactants into the combustion chamber.

String shear zones associated with these flow features generate vorticity between the recirculation zones, the jet, and the wall. Ultimately, the vorticity generated by these flow features has a large effect on local flame behavior, and thus, the dynamics of flame-vortex interactions are expected to be a major contributor to thermoacoustic instability [12].

Sufficiently small vortices will tend to pass through the flame without greatly perturbing it, but larger vortices will induce perturbations in the flame surface area by wrinkling the flame, and thus resulting in greater heat release. Still larger vortices will tend to induce flame roll-up, increasing both flame surface area and heat

release. Convection of these vortices can result in convecting pocket of burning reactants. These interactions with large vortices provide one mechanism for increased heat release.

1.4 Suppression and Control of Instability

As noted in §1.1, thermoacoustic instabilities owe their existence to a positive feedback loop coupling heat release and acoustic oscillations. The aim of any technique developed for instability suppression is to break this feedback loop, and prevent the system from pumping energy into these oscillations at the same frequency as the oscillations themselves. There are two categories of control strategies that have been explored: active and passive.

Active control is characterized by the expenditure of energy from an external source in an effort to prevent the combustor from significantly deviating from a desired operating condition. Active control can be either open-loop or closed-loop, and a substantial amount of research is devoted to developing the sensors, actuators and algorithms necessary to make these methods viable.

One of the major drawbacks of active control in general is the heavy reliance on complicated, interdependent components. In addition to developing appropriate actuators needed for open-loop control, closed loop control must also rely on the stability of algorithms and the robustness of sensors [13, 14, 15]. Actuation for active control system is often accomplished through acoustic forcing [16], fuel modulation, or through other novel techniques. Many active control methodologies have proven to be both feasible and scalable, although they have yet to be widely adopted in practical combustors.

Unlike active control, passive control strategies attempt to modify the fundamental dynamics of the combustion system in order to break the coupling between heat release and chamber acoustics, or to suppress unstable modes. Among these methods, the use of acoustic damping mechanisms, such as Helmholtz resonators have been shown to be effective, but are each only capable of suppressing instability in a narrow

frequency range, and are impractical for use in systems such as aircraft where low mass is a priority [17, 15].

Other techniques have looked at fuel staging or secondary ("pilot") fuel injection, to dynamically stabilize the flame. Although these strategies have met with some success in terms of reducing or eliminating combustion instability, they have done so at the cost of reduced emissions gains, due to higher flame temperatures in the combustion of locally richer fuel mixtures.

1.5 Thesis Goals

Combustion instability is a major challenge facing the development of combustors that operate in the fully-premixed mode, preventing new designs from reaching their full potential for the reduction of NO_x emissions. Most commercial combustors have complicated geometries, designed to address practical concerns of weight, cost, and heat transfer, among others. Nevertheless, many still employ swirl as a mechanism for flame anchoring and mixing, and are sucsceptible to a variety of longitudinal and transverse modes of instability. This instabilities arise due to the coupling of heat release, chamber acoustics, flow dynamics and equivalence ratio oscillations.

In this thesis, a swirl combustor with simplified geometry is studied with the intent of isolating and elucidiating some of the fundamental mechanisms that drive longitudinal instabilities. In particular, the mixing process was decoupled from the chamber acoustics, and thus, instabilities due to processes in a constant equivalence ratio combustion environment were studied.

The present work was divided into two segments: an experimental examination of the physical mechanisms leading to dynamic combustion stability and instability, and an experimental development and assessment of a technology for passive instability suppression. These two aspects were coupled, and what follows in the rest of this thesis is an analysis of the data gathered through acoustic and optical measurements of both the baseline combustion system and the microjet stabilized system.

Chapter 2 details the design of the experimental equipment and procedures. The

design of the combustor is discussed in detail along with the diagnostic techniques. The challenges associated with applying stereoscopic PIV to a reacting flow in a cylindrical combustion chamber, as well as the specific steps that were taken in order to address these challenges are discussed in sufficient detail to provide a starting point for future PIV studies of reacting flows. A discussion of the microjet design is left to §4.1, where the injector designs are discussed in the context of their intended and actual effects.

Chapter 3 explores stability and instability in the baseline combustor. A one-dimensional acoustic model is presented, followed by the analyses of three distinct operating regimes: lean, stable operation; one-quarter wave instability; and three-quarter wave instability. Stereoscopic PIV and chemiluminescence data, synchronized with acoustic data. Particular attention is paid to the dynamics of vortex breakdown and interaction between the flame and toroidal vortices in both the inner and outer recirculation zones.

In Chapter 4, modifications to the acoustic model are considered to account for the addition of mass and momentum to the combustor in the flame anchoring region. Following the presentation of this model, a description of the design and intended physical effect of eight different microjet injector configurations is given. The actual effect of microjet injection is subsequently compared with the theoretical model. Under certain conditions, microjets were effective in suppressing or eliminating combustion instability. An example of this operating mode is examined in detail, with stereoscopic PIV, chemiluminescence and acoustic measurements.

Chapter 5 summarizes the contributions of this work and presents recommendations for future research.

Chapter 2

Experimental Setup

Experiments were carried out in the Reacting Gas Dynamics lab, making use of a pre-existing experimental combustor setup. A custom MATLAB script was used to control the operating conditions of the combustor and record data from pressure sensors. Commercial software applications, GXLINK and DaVis 7.2, were used to record data from high-speed digital cameras for flame images and PIV, respectively. Custom MATLAB scripts along with custom software written in Python using the NumPy, SciPy and MatPlotLib libraries were used for post-processing of data.

2.1 Swirl Stabilized Combustor Design

The combustor used for this experiment (Fig. 2-1) is a laboratory scale, atmospheric pressure, swirl-stabilized combustor with complete fuel/air premixing.

Inlet air is delivered from an external compressor, capable of delivering 0.110 kg/s of air at 883 kPa, through an inlet pipe with a diameter of 38 mm. Two separate Sierra C100M mass flow controllers allow for the injection of both a primary fuel (typically C_3H_8 or CO) and a secondary fuel (typically H_2). The mass flow controllers have an uncertainty of $\pm 1\%$. Downstream of the fuel injection, the flow is choked. The choke plate prevents pressure oscillations from inducing differential flow rates in the fuel and air, thus maintaining a constant equivalence ratio.

An axial swirler is located 40 cm downstream of the choke plate. The swirler (Fig.

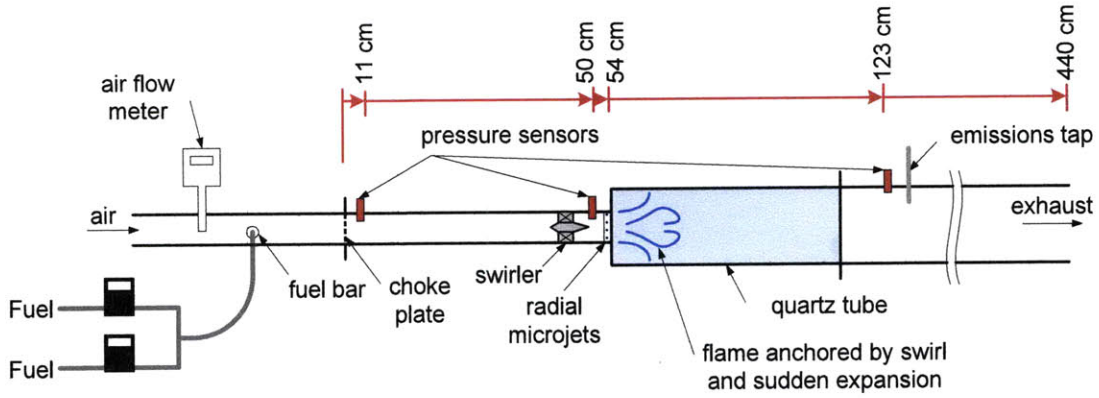

Figure 2-1: Schematic of the experimental, laboratory-scale, swirl-stabilized combustor.

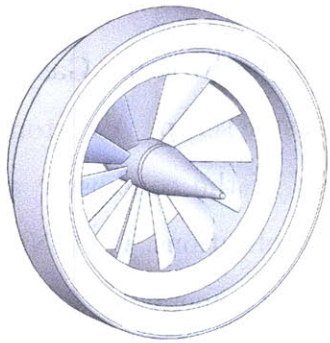

Figure 2-2: Solid model of main flow swirler.

2-2) consists of 12 thin cambered airfoils with a streamlined centerbody. The swirler induces positive swirl (clockwise, as viewed from upstream). The mean measured swirl number, based on stereoscopic PIV measurements in a non-reacting flow, is $\overline{S}$=0.53, calculated by

$$\overline{S} = \frac{(1/L)\int_0^L G_\theta \, dz}{(1/L)\int_0^L G_z R_0 \, dz} \tag{2.1}$$

where z is the axial coordinate, and L=76 mm is the axial extent of the viewing window for the PIV measurement. The igniter is located immediately downstream of the swirler.

A sudden expansion from the 38 mm diameter inlet pipe to 76 mm in the combustion chamber is located 54 cm downstream of the choke plate. The combustion chamber is an optically accessible quartz tube, approximately 50 cm long, which leads into a steel exhaust tube. Downstream of the combustion tube, the combustor ex-

pands into an exhaust pipe. The exhaust is vented into a large trench at a pressure slightly lower than atmospheric. The overall acoustic length of the combustor is 4.4 m.

Microjet air injectors, which will be discussed in detail in §4.1, are located near the expansion plane. Of the eight microjet injector configurations that were studied, three placed the air injection at the exit plane, and the remaining five placed the air injection approximately 5 mm upstream of the expansion.

Flow rate is set by the inlet Reynolds number, which is defined as

$$Re_{in} \equiv \frac{\rho_{mix} u_{in} d_{exp}}{\mu_{mix}} \tag{2.2}$$

where ρ_{mix} and μ_{mix} are the density and viscosity of the fuel-air mixture, respectively, and u_{in} and d_{exp} are the inlet flow velcity and the change in diameter at the sudden expansion, respectively. Mixture properties are calculated from temperature correlations based on all species in the mixture.

2.2 Experimental Procedures and Considerations

Combustion dynamics are highly non-linear in nature, admitting strong hysteresis as operating conditions are changed. The primary variable of interest in these experiments was the equivalence ratio (φ). The equivalence ratio is defined as the fuel/air ratio normalized by the stoichiometric fuel/air ratio at the choke plate, given by

$$\varphi = \frac{\left(\frac{\dot{m}_{fuel}}{\dot{m}_{air}}\right)}{\left(\frac{\dot{m}_{fuel}}{\dot{m}_{air}}\right)_{stoich}} \tag{2.3}$$

where the respective $\dot{m}$ terms are mass flow rates.

Of particular interest is the steady state dynamics of the combustor at different operating equivalence ratios. A standard testing procedure for this study was an *equivalence ratio sweep*, in which the equivalence ratio was systematically varied by a fixed $\Delta\varphi$ (normally $\Delta\varphi = 0.01$) between two operating points. Since the equivalence ratio is measured from the mass flow rate of fuel and air through the two flow

controllers, upstream of the chokeplate, it was necessary to allow sufficient time for the mixture to convect down to the combustion chamber, and for the dynamics to stabilize for the given equivalence ratio.

All tests were conducted at Re_{in}=19000 and T_{in}=300 K. At these conditions, a lower bound for the mass flow rate is $\dot{m}$=9.5 $\times$ 10^{-3} kg/s, which coupled with an inlet area of A=1.13 $\times$ 10^{-3} m^2 and a mean inlet density of ρ=1.2 kg/m^3, gives a mean flow velocity of u_{in}=7.0 m/s. This translates to a convective time of approximately τ_{in}=0.07 s for flow to propagate from the fuel injection sight to the flame anchoring zone. In order to obtain reliable acoustic data during the equivalence ratio sweeps, the equivalence ratio was held constant for at least an additional 2 s beyond the convective time during the sweep.

A consequence of the non-linearity in the system is hysteresis. Hysteresis is observed by noting changes associated with the direction of the equivalence ratio sweep.

An example can be seen in Figure 2-3. In both cases, the combustor is operated with a propane/air mixture, and ignited at an equivalence ratio of φ=0.70. In Fig. 2-3(c), the equivalence ratio is first decreased to φ=0.58, and then the sound pressure level is recorded as the equivalence ratio is increased to φ=0.78 in steps of $\Delta\varphi$=0.01. In Fig. 2-3(b), the equivalence ratio is raised to φ=0.78 and the sound pressure level is recorded as the equivalence ratio is decreased to φ=0.58 in increments of $\Delta\varphi$=0.01. A delay in the transition between modes can be seen, depending on the directionality of the sweep.

The cause of hysteresis is unknown and beyond the scope of this thesis. Heat transfer through the combustor walls to the upstream section of the combustion chamber may play a role. Kedia, *et. al.* [18], numerically demonstrated a resonant heat transfer phenomena wherein heat release oscillations transfer heat upstream into the inlet section, effectively preheating the inlet mixture and modifying the dynamics. It is conceivable that the persistence of the 110 Hz instability in Fig. 2-3(b) to lower equivalence ratios than in Fig. 2-3(c) may be influenced by a similar resonant heating phenomenon. Experimental verification of this or other phenomena which may account for the hysteresis would be difficult, and best performed in geometrically

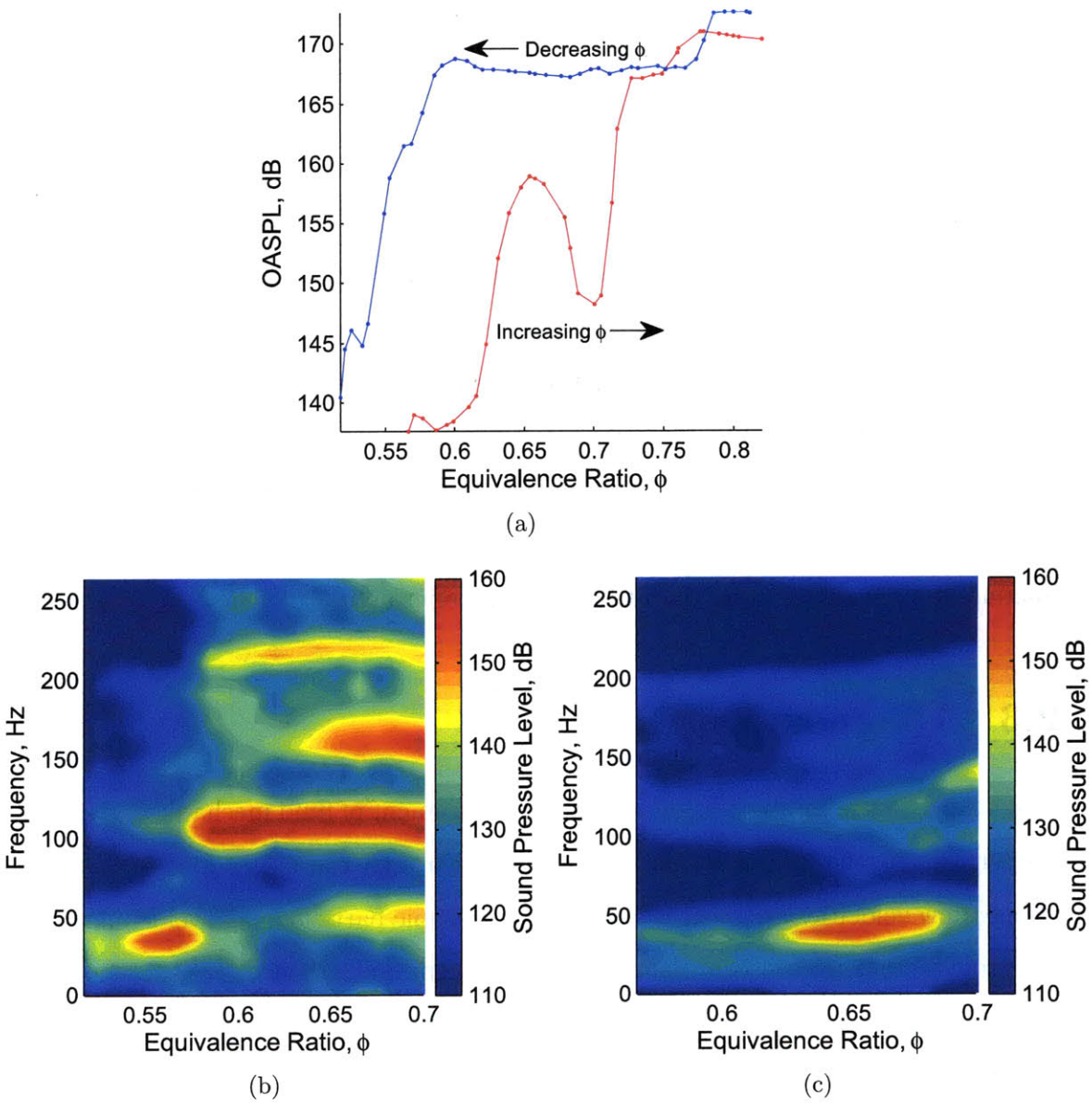

Figure 2-3: Overall sound pressure level (**a**) and sound pressure level spectra as a function of equivalence ratio in propane/air flame for decreasing equivalence ratio (**blue,b**) and increasing equivalence ratio (**red,c**).

simpler test rigs.

In order to isolate the data from these mechanisms of hysteresis, equivalence ratio sweeps were always conducted by increasing the equivalence ratio to its maximum value for the prescribed test conditions, allowing the dynamics to reach steady state, and recording data as the equivalence ratio was decreased.

For experiments in which a particular mode was examined via chemiluminescence or PIV, the equivalence ratio was first increased to its maximum value and then decreased to the target value and held fixed for the duration of the data recording. For experiments with active microjet air injection, the combustor was brought to its maximum equivalence ratio with the microjets off. Microjets were subsequently turned on, and data was recorded at the appropriate equivalence ratios. The equivalence ratio is reduced with microjet air injection due to dilution. In order to avoid exciting a higher mode and thus changing the initial flame dynamics at which the experiments were comducted, this means that all tests with microjets have a lower maximum equivalence ratio than tests without microjets.

2.3 Diagnostics

Diagnostics in the combustor focus on the measurement of fluid mechanic and acoustic properties. Acoustic oscillations are measured through the use of a sensitive microphone; flow velocities are measured using stereoscopic particle image velocimetry; and a surrogate heat release is measured through chemiluminescence.

External triggering of the acoustic recording system in the combustor control program and in the camera control software allow for acoustic and optical data to be temporally synchronized.

2.3.1 Pressure Measurement

Pressure measurements were made downstream of the of the choke plate at three locations: 11 cm downstream of the choke plate ($P1$), 4 cm downstream of the swirler ($P2$), and 79 cm downstream of the expansion ($P3$). Sensor locations are shown in

Fig. 2-1.

Sensors $P1$ and $P3$ are Kulite MIC-093 high-intensoty microphones. Sensor $P2$ is a Kistler 7076B water-cooled pressure sensor. $P2$ was flush mounted with the inside of the combustor. The two Kulite sensors, $P1$ and $P3$, are not capable of withstanding the high temperatures associated with combustion, and were offset from the main chamber of the combustor in semi-infinite line configurations. The acoustic length of the associated tubes was 30 m.

Data are acquired through a National Instruments PCIe-6259 data acquisition board at a rate of 10 kHz using the MATLAB data acquisition toolkit.

2.3.2 Flame Imaging

Flame imaging was achieved using a high-speed, digital CMOS camera. Images could be acquired at a maximum rate of 5 kHz. For unstable modes above 100 Hz, images were recorded at 2 kHz; for unstable modes below 100 Hz, images were recorded at 1 kHz; for stable modes of operation, flame images were recorded at 500 Hz.

Due to the axisymmetric nature of the flow, flame images show integrated light intensity values. Under the assumption of axisymmetry, at least in the average case, the light intensity as a function of radial position can be computed using an inverse Radon or inverse Abel transform. Under the assumption that the angle between the projected image and the viewing location is constant, the inverse Abel transform can be used to deconvolve the image [3]. This assumption is justified by noting that the maximum angle θ, from the camera to the sidewall of the quartz combustion chamber is approximately 4.5°. The principle of the inverse Abel transform is shown schematically in Fig. 2-4. An example flame image before deconvolution is shown in Fig. 2-5(a) and the flame image after deconvolution is shown in Fig. 2-5(b). The exact algorithm used can be found in [19].

Color balance wsa adjusted for all flame images included in this work to increase contrast for visual presentation. As such, the relative intensity between flame images from different data sets is not consistent, as presented in this work. All images within a given data set, such as the sequence of flame images for a particular mode, are

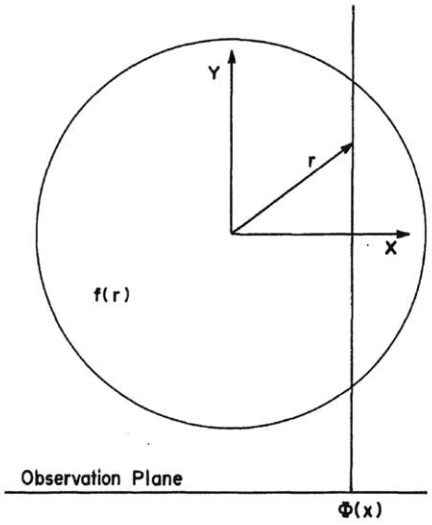

Figure 2-4: The inverse Abel transform computes $f(r)$ from the its projection $\Phi(x)$ [3].

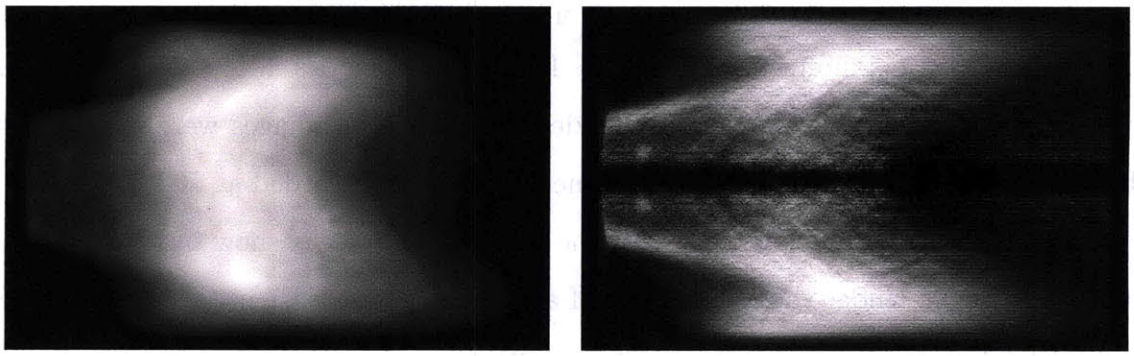

(a) (b)

Figure 2-5: Postprocessing of flame images show (a) a raw flame image and (b) a deconvoluted flame image. Deconvolution is achieved using the inverse Abel transform.

consistent.

2.3.3 Stereoscopic Particle Image Velocimetry

As a major part of this study, a stereoscopic particle image velocimetry (PIV) was setup and used to investigate flow dynamics inside the swirl combustor. High-speed cameras coupled with a high-power, pulsed laser enabled the measurement of time-resolved flowfield measurements. Although commonly used for fluid measurements, the application of PIV to a swirling, reacting flow presented several unique challenges.

As well as presenting the details of the PIV setup, this section discusses theese challenges and their solutions.

PIV techniques have been successfully applied to combustion (see [20, 21]), but the combination of the combustor's confined, cylindrical geometry, the swirling flow, and the reacting complicates the problem. In particular, in addition to the the strong thermal, velocity, and density gradients associated with reacting flows, in this setup, we also had to deal with internal reflections on the quartz combustion chamber and coating of the combustion chamber by seeding particles. Selection of seeding particles, reduction of reflections, and specific operating practices are all discussed below.

System Configuration

The midplane of the combustor was illumated using a pulsed Photonics Nd:YLF laser operating at 60 W, producing light at 527 nm (visible, green) and 1053 nm (infrared). The laser is directed through sheet-forming optics shown in to produce a laser sheet on the order of 1 mm thick as it passes through the combustor. Two high-speed digital cameras are mounted above the flame anchoring region of the combustor, approimately 15° from vertical. The distance between combustion chamber and lens is the same for both cameras to within 2 cm. A slight discrepancy is introduced due to asymmetries in the mounting hardware on the cameras, but this does not effect the quality of the calculations. Nikon 50 mm are used at an f-stop of 8 to maximize depth of field. *Scheinflug* adapters are used on each camera to compensate for the angle between the camera viewing direction and the normal to the light sheet. A two-plane calibration block was used for calibration. The camera and laser configuration is shown schematically in Fig. 2-6.

A cyclone-type seeder feeds seeding particles into the inlet pipe just downstream of the choke plate. Al_2O_3 particles were chosen to seed the flow; this choice is discusses in the following section.

Images were captured at a rate dependent on the mode of instability. Stable flame images were captured at 500 Hz, the low frequency (40 Hz) mode was recorded at a rate of 1000 Hz, and higher frequency instabilities (with 110 Hz and 160 Hz

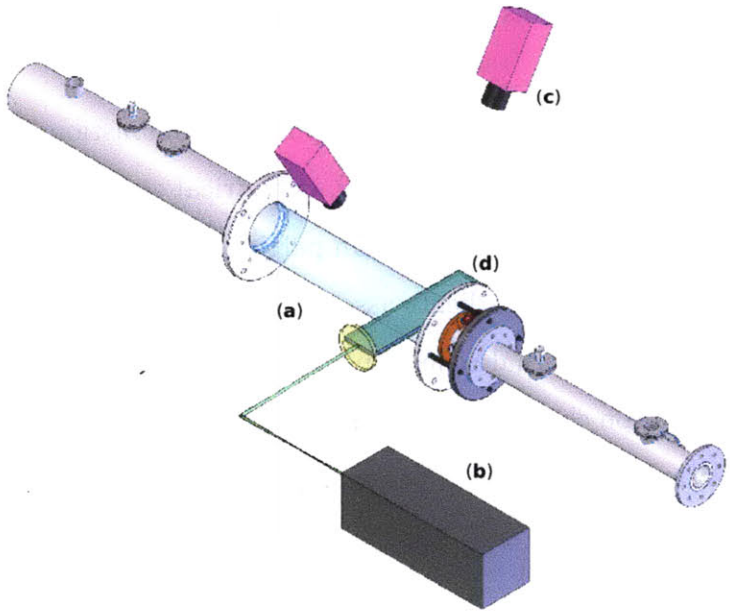

Figure 2-6: Schematic of optical diagnostic equipment: combustion chamber (**a**), illuminating laser (**b**), high-speed digital cameras (**c**), and laser light sheet (**d**).

components) were captured at 2000 Hz. Exposure time was 10 μs for all images.

Processing was done using commercial DaVis 7.2 software.

Seeding Particle Selection

The appropriate selection of seeding particles is one of the most challenging aspects of applying PIV to combustion applications. In non-reacting flows, seeding particles are chosen based both on their optical properties and on their ability to follow changes in flow velocity. This second property is affected by the ratio of density between the seeding particles and the fluid as well as the magnitude of accelerations in the flow. Often, in applications where the fluid being investigates is a gas such as air, smoke particle, styrofoam, or oil droplets are used for seeding. In a combusting flow, one of the major criteria is the survivability of the particle. Thermal stresses and high temperatures require the use of ceramics such as Al_2O_3 or TiO_2 among others. These ceramics are not ideal particles, due to the large density ratio between the particles and the combusting mixture, but are necessary to necessary to survive the flame.

On the length scales of seeding particles, the dominant force experienced by the

particles is Stokes drag. In the presence of a large temperature gradient near the flame, however, particles are subject to a separate *thermophoretic* effect of the form

$$F_{th} \propto -\frac{\mu^2}{\rho} d_p \frac{\nabla T}{T} \tag{2.4}$$

where μ is the fluid viscosity, ρ is the fluid density, d_p is the particle diameter and $\nabla T/T$ is the normalized temperature gradient. The force is opposite the direction of the temperature gradient.

Stella [22] showed that thermophoresis is the limiting factor in determining the maximum allowable size of the seeding particles. The concern was not the velocity lag due to thermophoresis, which was relatively small and assumed to average out, but the spatial shift in the velocity lag due to thermophoresis. For laboratory scale combustors with low flow velocities, Stella placed an upper bound of d_p=3 μm.

A final note on TiO_2 is that the scattering cross section is greatly reduced as the temperature increases. This effect has been considered as a means of marking the flame boundary. For the purposes of this research, however, TiO_2 was not chosen in order ease the computation of velocity vectors in the post-flame region.

Dealing with Specular Reflections

The cylindrical geometry of the combustor, coupled with the relectivity of quartz gives rise to multiple internal reflections in the quartz tube. These reflections can saturate the camera and obscure particle locations, and are particularly prominent in the presense of the high-power laser used for illumination.

Optical accessibility was only necessary through the upper part of the quartz chamber, below the cameras. In order to reduce internal reflections, the lower section of the tube, just below the mid-plane, was internally sandblasted. This process resulted in more diffuse reflections, and as shown in Fig. 2-7, reduced the overall severity of the reflections.

Traditional anti-reflective coatings such as Rhodamine are unable to withstand the high temperatures of combustion. In their place, a thin layer of graphite was

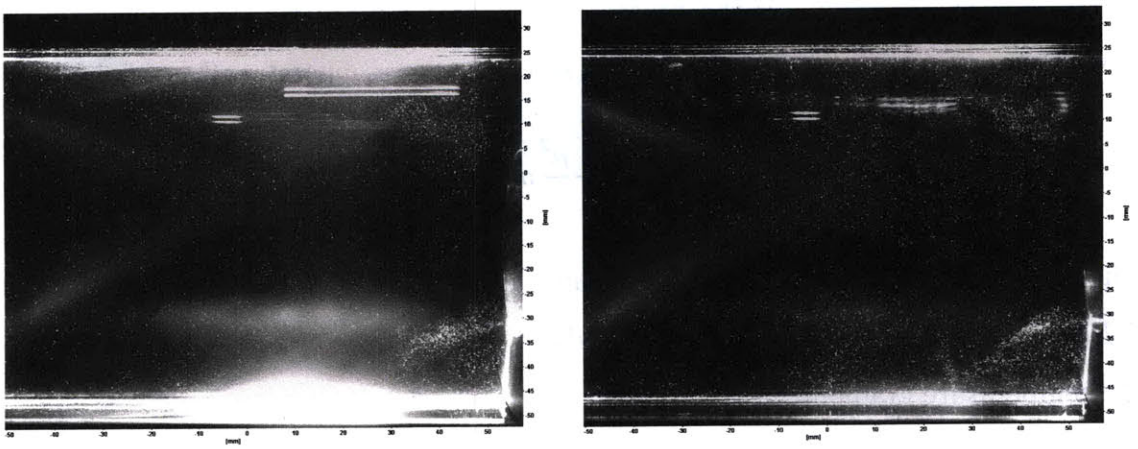

(a) (b)

Figure 2-7: High-speed photograph of internal reflections in an untreated quartz tube (**a**) and in a quartz tube which has been sandlasted on the lower section (**b**).

applied to any metal surface that contributed significantly to reflection problems.

Operational Considerations

In addition to the considerations mentioned above, another confounding problem that was encountered was the rapid coating of the inside wall of the quartz tube by seeding particles. A thin layer of seeding particles would completely obscure the flowing particles inside the tube, as shown in Fig. 2-8.

Static was eventually determined to be a major contributing factor to this problem. In order to prevent severe accumulation of particles, the tube was handled with anti-static gloves and the inside was wiped clean of particles with anti-static cloth between runs. Seeding was added gradually to the flow immediately prior to the recording images and shutoff immediately after.

2.4 Post-Processing

As a primary aim of this research was to study the role of coherent flow structures in thermoacoustic instability, the flame images and PIV data needed to be post-processed in order to separate the coherent structures from turbulent fluctuations in

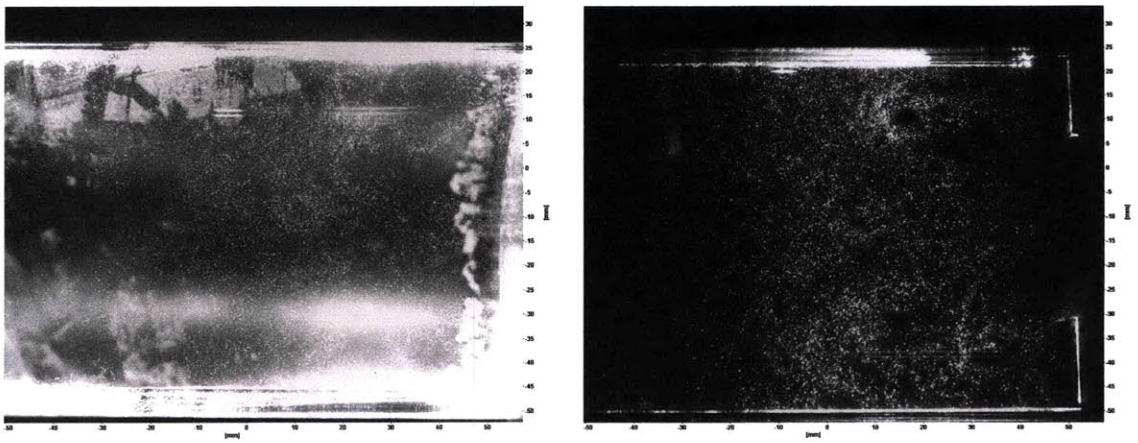

(a) (b)

Figure 2-8: Seeding particles rapidly accumulate on the inside of the combustor tube (**a**). Anti-static treatment and limited exposure to the particles reduces this problem, allowing data to be collected (**b**).

the flame surface and flow field. Sung [23] proposed the use of phase-averaging of periodic flows to study coherent structures.

Phase-averaging works in cases where a distinct periodicity in the system can be measured independently of the flame images and PIV data sets. High-speed images are synchronized at recording with the acoustic measurements. For unstable operating modes, the dominant acoustic mode determines the periodicity of the images. Images are sorted into 80 bins based on their relative phase, where they are averaged.

Chapter 3

Swirl Combustor Dynamics

The combustor, described in §2.1, was the subject of the first phase of this research. Various operating conditions, covering a range of stable and unstable modes were probed with optical and acoustic measurements.

Before examining the measurements that were made on the system, in §3.1, we will use a linearized, one-dimensional model of the combustor to identify and understand the theoretical acoustic modes of the combustion process, as well as the anticipated phase relationship between pressure and velocity oscillations for unstable operating conditions. In the subsequent sections, we will examine the measured values in the context of the predictions of this linearized model.

Flame images and PIV data are used to compute the phase relationship between the pressure, velocity and heat release oscillations for two unstable modes. The phase of the instantaneous heat release rate is estimated from the luminosity of the flame images. Pressure is measured using the sensitive Kulite microphone, $P1$ near the choke plate and corrected for the time lag to the combustion chamber using the upstream speed of sound. The acoustic velocity is the upstream (pre-flame) velocity. This is estimated from the velocity in the annular jet in the first 10 mm downstream of the expansion.

3.1 Theoretical Acoustic Model

A simplified model of the combustor has been developed by Speth *et al.* [24] investigated the phase relationship between heat release, acoustics, and axial velocity in the context of Rayleigh's criterion. The model is a quasi one-dimensional model based on the homogeneous acoustic wave equation applied between point sources of mass, momentum, velocity and heat. The framework for this type of model has been developed by McManus [25], Fleifil [26], Dowling and Stow [27], and others.

The model is based on the following assumptions:

1. the combustor is essentially one-dimensional;
2. the flame is compact compared to the acoustic length of the combustor;
3. the reactant and product gases are calorically perfect;
4. the Mach number of the mean flow is small;
5. and the flow is inviscid.

Although only the axial component of velocity and axial property gradient are considered, the effect of area changes on the mass flow is considered, making the model only quasi one-dimensional. As will be shown in the following sections, this model predicts the resonant modes of the combustor well. By explicitly ignoring three-dimensional effects, it allows us to asess the importance of these effects based on their impact on the dynamics.

We begin by assuming that fluid and flow properties can be written as the sum of a mean component (denoted by an overbar), and a perturbation (denoted by a superscript prime). For example, the flow velocity can be decomposed as

$$u(x,t) = \overline{u} + u'(x,t) \tag{3.1}$$

Ignoring second and higher order perturbations, the equations for conservation of

mass, momentum and energy can be written as

$$\frac{\partial \rho'}{\partial t} + \overline{u}\frac{\partial \rho'}{\partial x} + \overline{\rho}\frac{\partial u'}{\partial x} = 0 \tag{3.2}$$

$$\frac{\partial u'}{\partial t} + \overline{u}\frac{\partial u'}{\partial x} + \frac{1}{\overline{\rho}}\frac{\partial p'}{\partial x} = 0 \tag{3.3}$$

$$\overline{\rho}\overline{T}\left(\frac{\partial s'}{\partial t} + \overline{u}\frac{\partial s'}{\partial x}\right) = q' \tag{3.4}$$

respectively. Heat release is assumed to occur only at the flame location, and is modeled as a discontinuity. Under this assumption, conservaton of energy reduces to

$$\overline{\rho}\overline{T}\left(\frac{\partial s'}{\partial t} + \overline{u}\frac{\partial s'}{\partial x}\right) = 0 \tag{3.5}$$

By neglecting the entropy mode, $s' = 0$, the energy equation is trivially satisfied. Furthermore, if we assume $\overline{u} = 0$ (that is, that the mean flow is negligible), then the conservation equations for mass and momentum reduce to

$$\frac{\partial \rho'}{\partial t} + \overline{\rho}\frac{\partial u'}{\partial x} = 0 \tag{3.6}$$

$$\frac{\partial u'}{\partial t} + \frac{1}{\overline{\rho}}\frac{\partial p'}{\partial x} = 0 \tag{3.7}$$

The equation of state for a perfect gas is given by

$$p = \rho R T \tag{3.8}$$

Expanding in terms of mean values and pertubations, we obtain

$$\frac{p'}{\overline{p}} = \frac{\rho'}{\overline{\rho}} + \frac{T'}{\overline{T}} \tag{3.9}$$

The entropy constitutive relation for a perfect gas is given by

$$s - s_0 = c_p \ln\frac{T}{T_0} - R\ln\frac{p}{p_0} \tag{3.10}$$

which, by Taylor expansion, becomes

$$s' = c_p \frac{T'}{\overline{T}} - R \ln \frac{p'}{\overline{p}} \tag{3.11}$$

which can be rewritten as

$$\frac{T'}{\overline{T}} = \frac{\gamma - 1}{\gamma} \frac{p'}{\overline{p}} - \frac{s'}{c_p} \tag{3.12}$$

As before, we assume $s' = 0$ and combine (3.9) and (3.12) to obtain

$$\rho' = \frac{1}{\gamma R \overline{T}} p' = \frac{1}{\overline{c}^2} p' \tag{3.13}$$

Substituting (3.13) into (3.6), we obtain another expression for the conservation of mass, given by

$$\frac{1}{\overline{c}^2} \frac{\partial p'}{\partial t} + \overline{\rho} \frac{\partial u'}{\partial x} = 0 \tag{3.14}$$

Finally, we combine (3.7) and (3.14), obtaining

$$\frac{1}{\overline{c}^2} \frac{\partial^2 p'}{\partial t^2} - \frac{\partial^2 p'}{\partial x^2} = 0 \tag{3.15}$$

which is he homogeneous wave equation for acoustic waves.

Acoustic waves travel as plane waves in the one-dimensional combustor model. The general form is

$$p'(x,t) = f(t - x/\overline{c}) + g(t + x/\overline{c}) \tag{3.16}$$

and from continuity, the axial velocity can be expressed as

$$u'(x,t) = \frac{1}{\overline{\rho}\,\overline{c}} \left[f(t - x/\overline{c}) - g(t + x/\overline{c}) \right] \tag{3.17}$$

It will be convenient to decompose perturbations by frequency, writing

$$f(t) = Re \left[\hat{f} e^{i\omega t} \right] \tag{3.18}$$

where $\hat{f}$ is a complex amplitude. Next, the appropriate boundary conditions are

applied to obtain the resonant modes of the system.

Boundary Conditions

We now have a framework for the modeling acoustic waves in a homogeneous media. We can split the combustor into three sections, and apply these equations in each section using the appropriate boundary conditions. The three sections are: (1) the section between the choke plate and the sudden expansion, (2) the section between the sudden expansion and the flame, and (3) the section between the flame and the exhaust. The inlet of the combustor is located at $x = 0$, the expansion at $x = L_e$, the flame at $x = L_f$, and the exhaust at $x = L$.

The open end at $x = L$ is assumed to be a pressure node, $\hat{p}(L,t) = 0$, and the choked inlet at $x = 0$ is assumed to be a pressure antinode, $\partial\hat{p}/\partial x|_{x=0,t} = 0$. The jump condition at $x = L_e$ is given by

$$\hat{u}_2 = \frac{A_1}{A_2}\hat{u}_1 \tag{3.19}$$

The heat release oscillations q' at $x = x_f$ are assumed to be proportional to time-lagged pressure oscillations

$$q'(t) = \Lambda p'(L, t-\tau) \tag{3.20}$$

where Λ is the constant of proportionality and τ is the time lag. To satisfy Rayleigh's criterion, we assume that $\tau \approx 0$, yielding

$$q'(t) = \Lambda p'(L_f, t) \tag{3.21}$$

The velocity jump across the flame is given by

$$\hat{u}_3 = \hat{u}_2 + \frac{\gamma - 1}{\bar{\rho}_2 \bar{c}_2^2} q'(t) \tag{3.22}$$

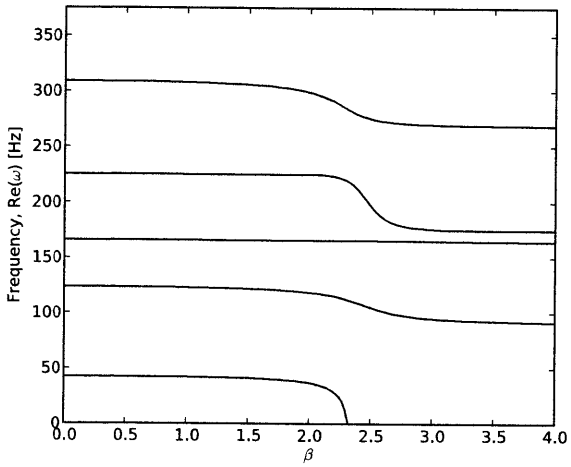

Figure 3-1: Resonant frequencies of the combustor as a function of the heat release parameter β.

which can be expressed as

$$\hat{u}_3 = \hat{u}_2 + \frac{\gamma - 1}{\overline{\rho}_2 \, \overline{c}_2^2} \Lambda p'(L_f, t) \tag{3.23}$$

Defining the dimensionless heat release parameter $\beta \equiv (\gamma - 1)\Lambda/\overline{c}_2$, the final form of the jump condition is

$$\hat{u}_3 = \hat{u}_2 + \frac{\beta}{\overline{\rho}_2 \, \overline{c}_2} \hat{p}_2(L_f, t) \tag{3.24}$$

This yields a system of equations for the ω, $\hat{f}$, and $\hat{g}$.

Resonant Modes

By substituting (3.18) and (3.16) into (3.14) and solving for ω, we can find the resonant frequencies of the combustor as a function of the heat release parameter β. For values of the heat release parameter β <2.3, we expect a 1/4 wave mode near 40 Hz, a 3/4 wave mode near 120 Hz, and a 5/4 wave mode near 160 Hz, as shown in Fig. 3-1.

A Note on Secondary Air Injection

The model presented above is based on the conservation equations for an ideal fluid. In particular, if we consider two regions, (1) upstream and (2) downstream of the injection point, the conservation of mass becomes

$$\rho_2 u_2 A_2 = \rho_1 u_1 A_1 + \dot{m}_{mj} \tag{3.25}$$

where A_1 is the area of the combustor upstream of the injection point, A_2 is the area of the combustor downstream of the injection point, and $\dot{m}_{mj}$ is the total mass flow rate through the microjets.

Conservation of momentum must be handled with care. Although radial microjets inject mass, they inject no *axial* momentum into the flow, and hence, there is no change to conservation of linear momentum. Axial microjets do inject axial momentum, and the new form of the conservation law becomes

$$\rho_2 u_2^2 A_2 = \rho_1 u_1^2 A_1 + \frac{\dot{m}_{mj}^2}{\rho_{mj} n A_{mj}} \cos^2\theta \tag{3.26}$$

where ρ_{mj} is the density of the secondary air, n is the number of microjet injector ports, A_{mj} is the area of a single injector port, and θ is the angle between the microjet injector and the axis of the combustor.

In the context of the acoustic model, a distinction is made between mean flow variables and pertubations that vary in time and space. In particular, as noted by Fleifil [26] and Dowling [27], acoustic oscillations can arise as a coupling between $p'$and q', or between p' and $\dot{m}'$, and so mass fluctuations are important, as well as pressure and velocity fluctuations.

A more rigorous derivation of this model, presented by Fleifil, found that in the absence of entropy fluctuations and heat transfer, the acoustic energy is given by

$$\frac{\partial}{\partial t}\int_V e' dV = \frac{1}{\bar{\rho}}\int_V p'\dot{m}' dV + \frac{\gamma - 1}{\bar{\rho}\,\bar{c}^2}\int_V p' q' dV - \phi \tag{3.27}$$

where e' is the energy density of the acoustic wave in the volume V, and ϕ is a viscous

loss term. We observe the under the assumptions of the model, which we also assume to hold in the case of microjet injection, the mean flow velcity ($\overline{u}$) and the mean mass flow rate ($\overline{\dot{m}}$), do not factor into the acoustic energy.

Choked microjets, therefore, do not have an impact on the acoustic modes of the system.

Implications

This model does not predict the conditions under which we will observe unstable modes, but it does predict what those modes will be. These modes are in reasonable agreement with those that we observe. The 3/4 wave mode is observed between 100 Hz and 110 Hz, depending on the exact inlet conditions, compared to 120 Hz predicted by the model; the 1/4 wave mode and 5/4 wave mode both resonate near the frequencies predicted in this model. This indicates that

1. the modes that we observe are longitudinal modes;

2. and the dynamics that govern these modes are essentially one-dimensional.

What we also note is that any change that we are able to effect in the behavior of the system by through secondary microjet air injection, is not accomplished through modification of the longitudinal acoustics of the system, but through more compex changes to the flow structure and the dynamics of the vortex breakdown.

3.2 Experimental Acoustic Behavior

In §3.1, the modes of the combustor were predicted using a one-dimensional, linear theory. This model provides useful data regarding the type of instabilities that may be encountered, but it makes no prediction for when a given mode will be observed, only what it will look like *if* it is observed. It has already been noted, in §2.2, that the combustor exhibits strong hysteresis. This alone is enough to inform us that the linear theory is not fully adequate. The purpose of this section is to outline the observed acoustic modes of the combustor near the lean limit.

For these experiments, the Reynolds number, based on the change in diameter at the expansion, is held constant at Re=19000, and the inlet temperature is fixed at T_{in}300 K. Two categories of fuel composition are considered: pure propane (C_3H_8), and syngas mixtures ranging from 20% CO and 80% H_2 to 80% CO and 20% H_2 by volume. As noted in §2.2, for all equivalence ratio sweeps equivalence ratio is raised to its maximum value, and then data is recorded and the equivalence ratio is slowly decreased.

Acoustic data are recorded, and the overall sound pressure level (OASPL) computed. The OASPL is given by

$$OASPL = 10 \log_{10} \overline{\left[\frac{p(t) - \overline{p(t)}}{p_0} \right]^2} \tag{3.28}$$

where the overbars denote time averages over a fixed Δt, $p(t)$ is the measured pressure signal, and p_0 is 2×10^5 Pa. Additionally, the sound pressure level at particular frequencies can be computed by appropriately filtering the $p(t)$ signal.

The acoustic behavior for the propane/air flames is shown in Fig. 3-2. Pressure is plotted at three locations - immediately downstream of the choke plate, immediately upstream of the expansion, and far downstream of the expansion - in Fig. 3-2(a). The combustor is unstable for all but very lean equivalence ratios. In Fig. 3-2(b), the sound pressure level is plotted as a function of the equivalence ratio and the frequency. This plot shows that, although the OASPL remains high, the combustor transitions to lower modes of instability as the φ is decreased. In particular, the phase relationship between the three pressure sensors changes abruptly at φ=0.58, marking a transition between the one-quarter wave mode and the three-quarter wave mode.

The acoustic response of the swirl combustor to equivalence ratio for different syngas/air flames is shown in Fig. 3-3. The OASPL and pressure maps are shown for four syngas mixtures with different CO and H_2 fractions are investigated.

Syngas exhibits very different behavior. High CO mixtures show transitions similar to those observed in the propane/air flames. The three-quarters wave mode resonates at 100 Hz, slightly lower than in propane/air flames. The 40 Hz mode is

weaker and occupies a smaller interval of the equivalence ratio range. For high H_2, the general trend is toward higher frequency modes of instability. The 40 Hz mode is not observed at all for syngas mixtures with more than 20% H_2. A higher frequency mode (160 Hz), which is observed in conjunction with the 110 Hz mode in propane is very prominent at higher equivalence ratios. For very high H_2 (80%), a pure 240 Hz mode is observed for equivalence ratios in the range $0.37 \leq \varphi \leq 0.42$. Below $\varphi = 0.37$, there is a stable regime. The 100 Hz mode is observed over a very narrow band, $0.26 \leq \varphi \leq 0.27$.

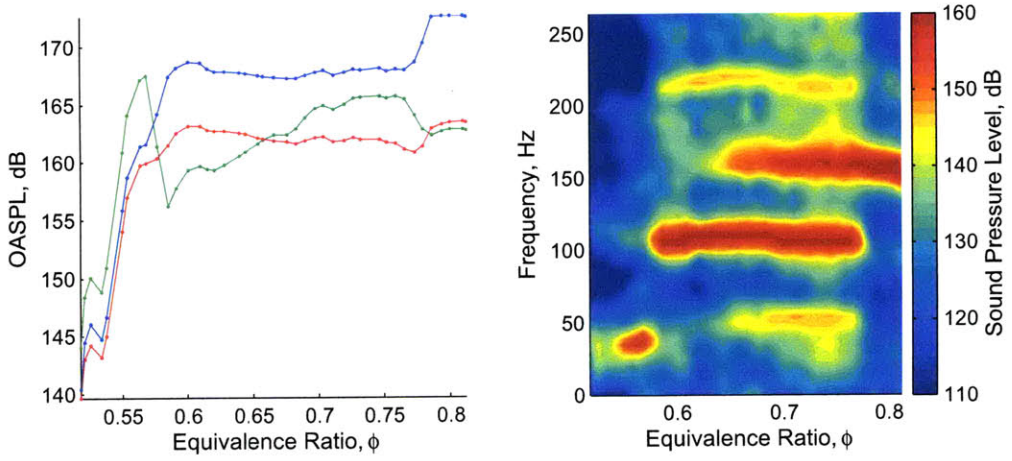

(a) (b)

Figure 3-2: Experimental acoustic modes for propane/air flames showing OASPL (**a**) and the sound pressure level spectrum (**b**).

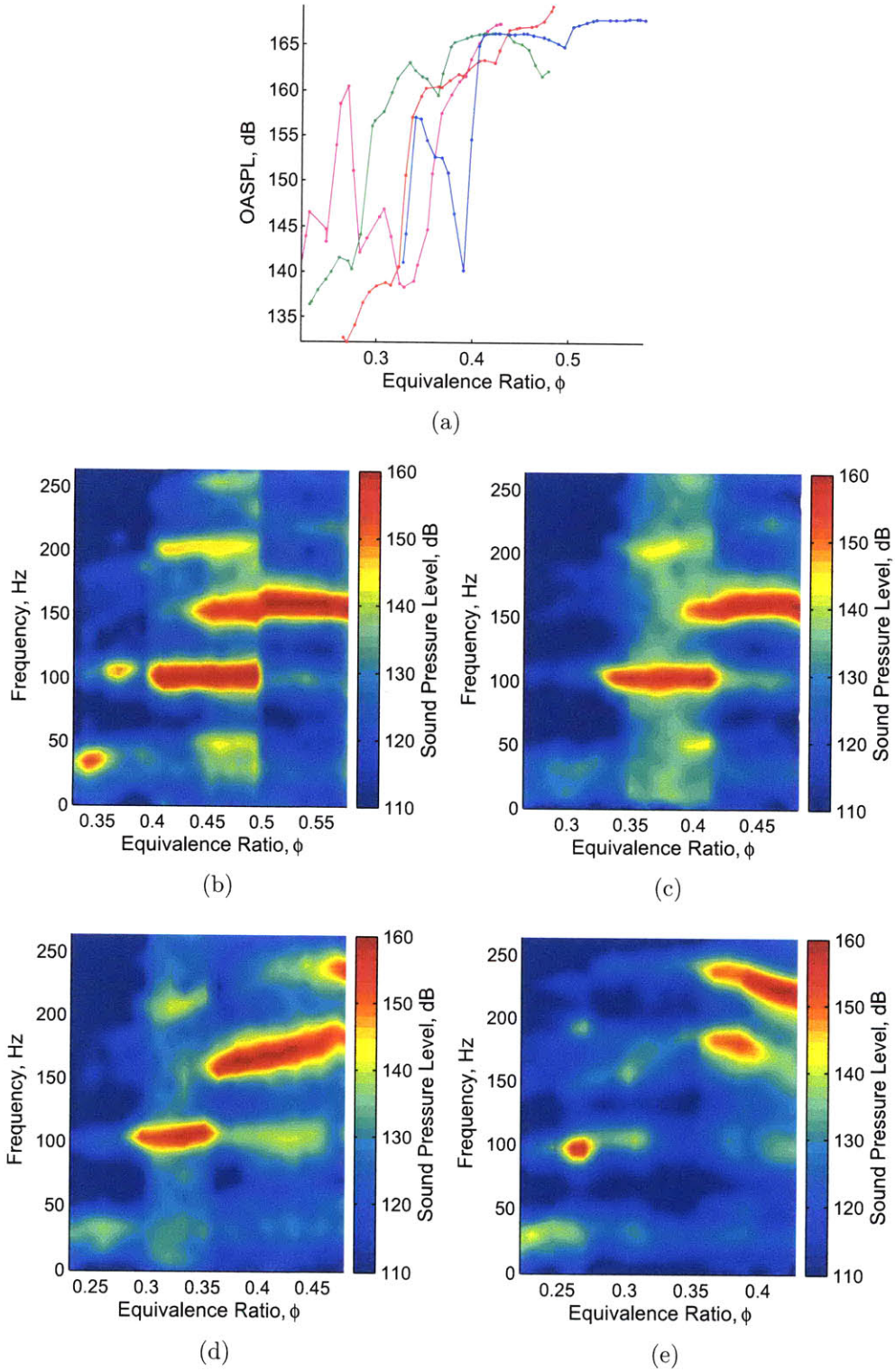

Figure 3-3: Experimental acoustic modes for syngas/air flames showing OASPL (**a**) and sound pressure level spectra for 80%/20% CO/H_2 (**blue,b**), 60%/40% CO/H_2 (**red,c**), 40%/60% CO/H_2 (**green,d**), and 20%/80% CO/H_2 (**magenta,e**) at Re=19000 and T_{in}=300 K.

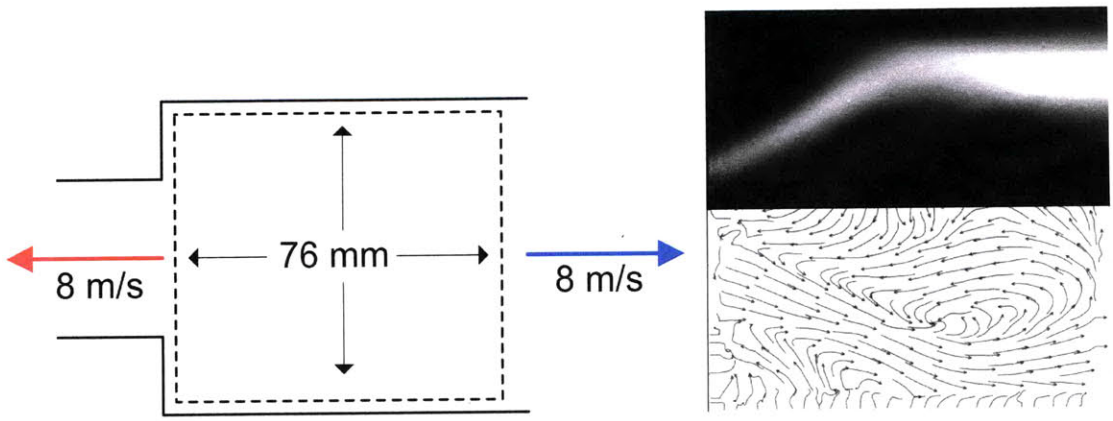

Figure 3-4: Time-average conical flame (**top**) and streamlines (**bottom**) at φ=0.70 (ignited lean) at Re=19000 and T_{in}=300 K for a propane/air micture.

3.3 Stable Flame

The flow field of the stable flame is shown in Fig. 3-4. The inner circulation zone, which is an instance of the two-cell vortex breakdown bubble discusses in §1.2, is bounded by an annular jet at the edge of the inlet pipe. The recirculation zone deflects the jet outward, and it eventually impinges on the wall. An outer recirculation zone exists between the corner of the combustion chamber and the jet. For the reacting flow, the flame is anchored between the inner recirculation zone and the jet. As the jet impinges on the wall of the combustion chamber, it carries reacting flow downstream, and the flame is seen to extend several diameters downstream of the expansion. Heat release, estimated from the luminosity, is seen to be higher along the wall than in the conical region for the flame. The flame length is estimated as ℓ_f=220 mm (see Fig. 3-5). The mean axial flow velocity in the viewing window is $\bar{u}_{st}$=1.7 m/s.

The overall sound pressure level in the combustor is on the range of 140 dB to 150 dB depending on the precise operating conditions (accounting for equivalence ratio and hysteresis).

The inner circulation zone, formed by a two-cell vortex breakdown bubble (discussed in §1.2), is bounded by an annular jet at the edge of the inlet pipe. The recirculation zone deflects the jet outward, and it eventually impinges on the wall. An outer recirculation zone exists between the corner of the combustion chamber

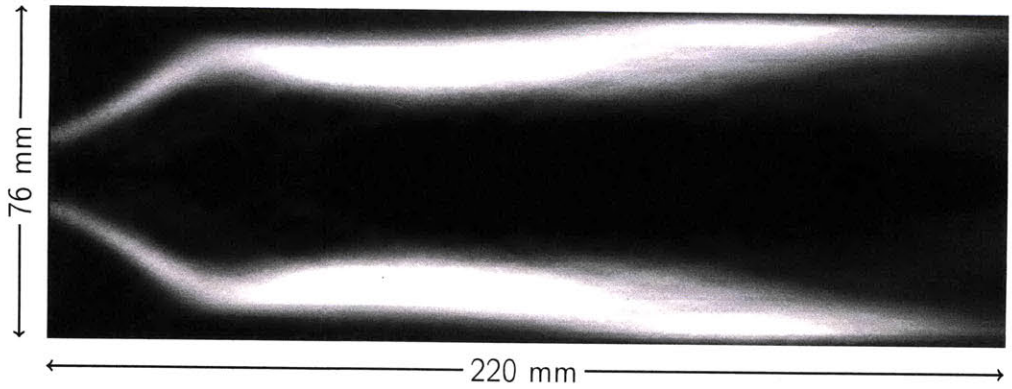

Figure 3-5: Time-average stable flame at φ=0.70 (ignited lean) at Re=19000 and T_{in}=300 K.

and the jet. The flame is anchored between the inner recirculation zone and the jet. As the jet impinges on the wall of the combustion chamber, it carries reacting flow downstream, and the flame is seen to extend well several diameters downstream of the expansion.

3.4 1/4 Wave Mode

The one-quarter wave mode is manifested as a 40 Hz acoustic oscillation (see the frequency spectrum in Fig. 3-6). This mode is observed at low equivalence ratios, below those at which the three-quarter wave mode is excited. Strong oscillations (greater than 150 dB) are obsereved in propane/air and high-CO syngas/air flames. Additionally, the mode is observed in low-CO syngas/air flames while counter-swirling radial microjets are active.

The outer recirculation zone and annular jet remain fixed in space throughout the cycle of the instability. Vortex breakdown of the incoming flow creates an annular vortex located inside the annular jet, downstream of the point where it impinges on the chamber wall. This vortex also remains fixed in space throughout the cycle, and contributes the reverse flow that creates the inner recirculation zone. Each cycle, an annular vortex with the opposite sense of swirl is shed upstream of the expansion. This vortex is convected downstream, and is responsible for periodic fluctuations in the strength of the inner recirculation zone. Due to this vortex, the core of the inner

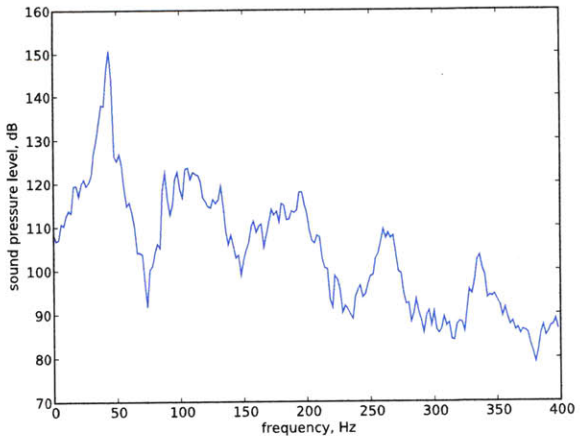

Figure 3-6: Frequency spectrum of the 1/4 wave mode measured at $P1$ at φ=0.56 with T_{in}=300 K and Re=19000.

recirculation zone forms a weak jet for part of the cycle.

In Fig. 3-8 and Fig. 3-9, phase-averaged flame images and streamlines are presented at several points throughout one cycle of the instability. The vortex shedding can be seen in Fig. 3-9(b), and it convects downstream, finally convecting outside of the viewing region by the next cycle, as shown in Fig. 3-8(b). The flame is anchored at the centerbody of the swirler, extending downstream along the leading edge of the inner recirculation zone, where combustion products are recirculated into the fresh reactants that are carried into the combustion chamber by the annular jet. We see the flame extend upstream of the point where the jet impinges on the wall, anchoring along the outer recirculation zone and the jet, and along the wall in the outer recirculation zone. The flame extends downstream of the inlet by 200 mm, as shown in Fig. 3-7, throughout the cycle.

The acoustic model implicitly assumes no phase shift between the pressure and the heat release rate oscillations. However, from Equation (3.16) and Equation (3.17), we expect there to be a 90° phase shift between the pressure and the acoustic velocity. The form of the solution admits both a lead and a lag.

We observe that the relationship between the acoustic velocity oscillations and the pressure oscillations is slightly greater than 90°, with the velocity leading the pressure. The heat release oscillations lead the pressure oscillations by approximately

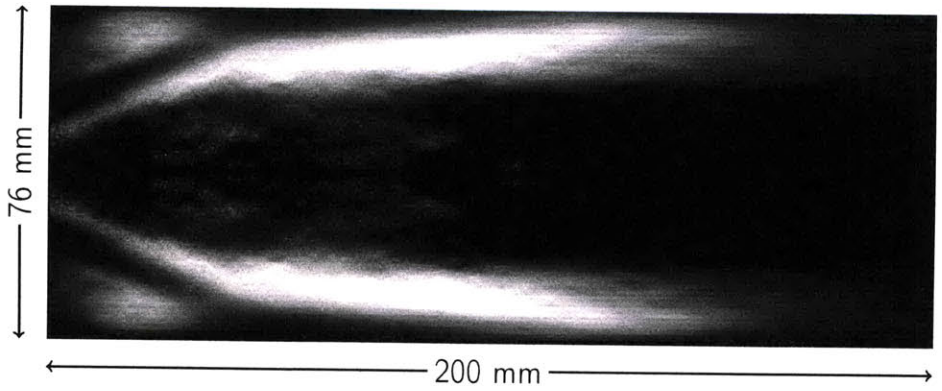

Figure 3-7: A typical phase-averaged flame for the 1/4 wave mode at the point of maximum heat release rate at φ=0.56 at Re=19000 and T_{in}=300 K.

70°. This violates the explicit assumption of no phase difference made in the acoustic model, but does satisfy the Rayleigh criterion. Importantly, Fig. 3-8 and Fig. 3-9 show us that the acoustic, inlet flow, and heat release rate all oscillate at the *same* frequency.

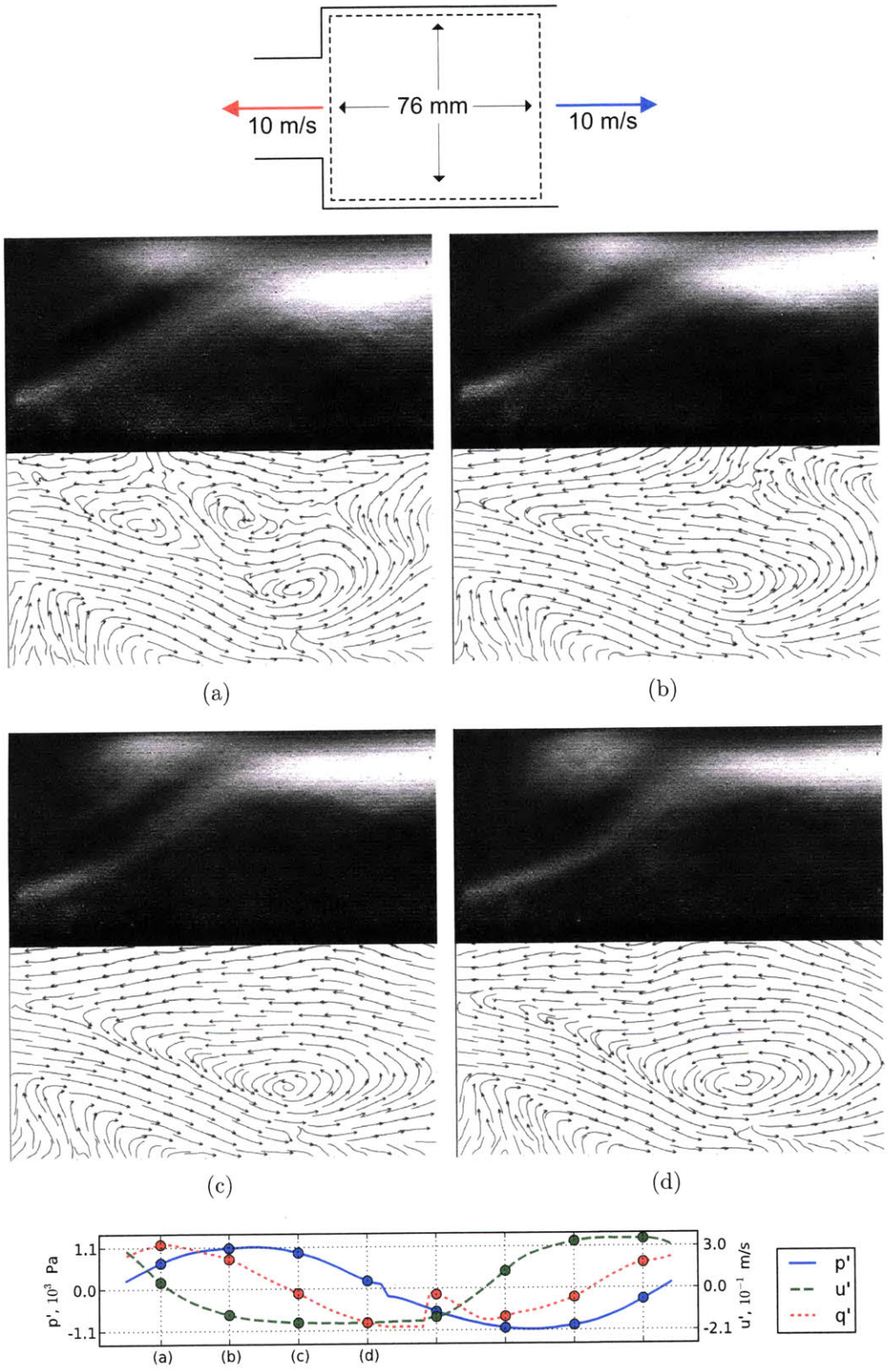

Figure 3-8: Flame images (**top**) and streamlines (**bottom**) for the 1/4 wave instability (first half of cycle). Measurements taken at Re=19000, T_{in}=300 K and φ=0.56.

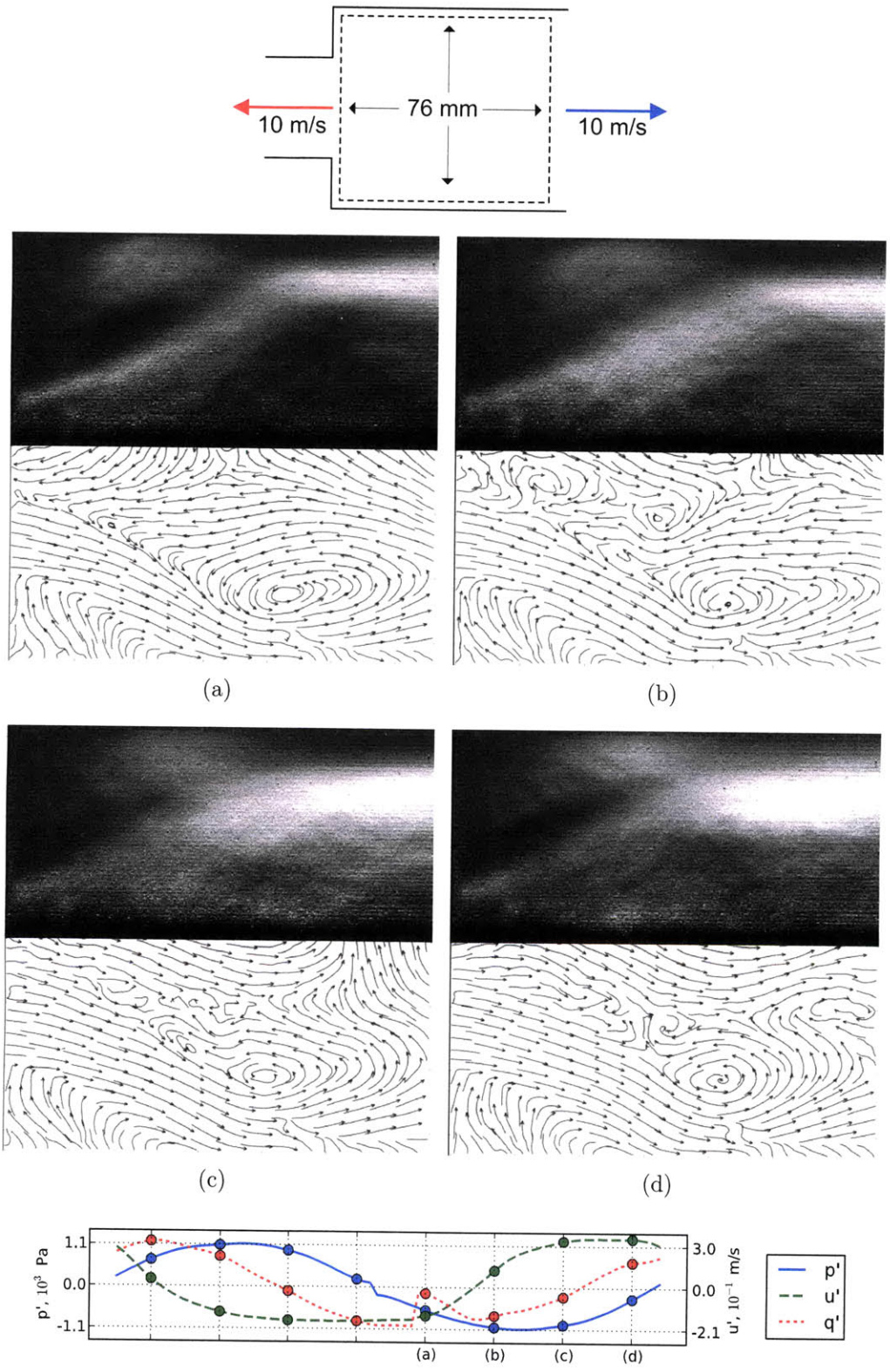

Figure 3-9: Flame images (**top**) and streamlines (**bottom**) for the 1/4 wave instability (second half of cycle). Measurements taken at Re=19000, T_{in}=300 K and φ=0.56.

3.5 3/4 Wave Mode

The 3/4 wave mode of the combustor oscillates with a dominant frequency of 105 Hz. A typical spectrum for this mode is shown in Fig. 3-10. For propane/air flames, this mode is observed over a large range of lean equivalence ratios, $0.58 \leq \varphi \leq 0.77$. Above φ=0.66, it is accompanied by a strong 160 Hz component. This mode is also prominent in syngas/air flames, particularly for high-CO syngas air flames. For low-CO, a pure 160 Hz mode persists over a greater extent of the operating range. Strong acoustic oscillations, on the order of 162 dB are observed at this frequency.

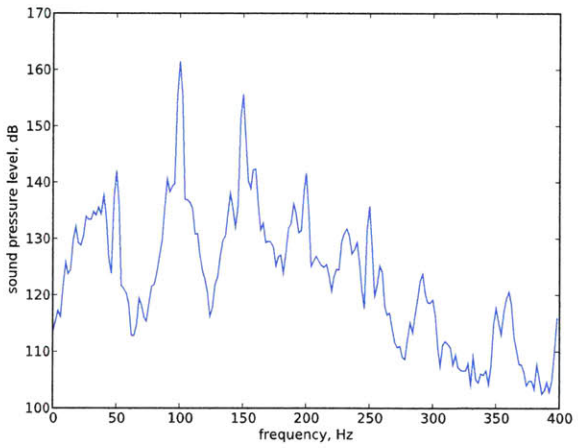

Figure 3-10: Frequency spectrum of the 3/4 wave mode measured at $P1$ at φ=0.75 with T_{in}=300 K and Re=19000. Both 105 Hz (at 161 dB) and 160 Hz (at 157 dB) frequencies are observed.

The 3/4 wave mode is characterized by very active flame and flow dynamics, and a significantly more compact flame. The flame extends downstream of the combustion chamber inlet between 70 mm at the point of minimum heat release in the cycle and 120 mm at the point of maximum heat release in the cycle, as shown in Fig. 3-11.

Phase-averaged flame images and streamlines are shown in Fig. 3-12 (the first half of the cycle) and Fig. 3-13 (the second half of the cycle). The sequence shows complex interactions between the flame and the dynamics of the inner and outer recirculation zones.

1. At the point of maximum heat release rate, a large annular vortex is observed

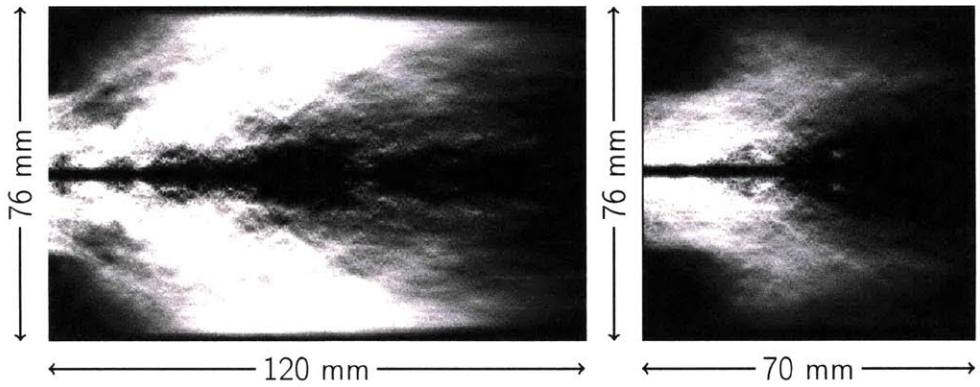

Figure 3-11: A typical phase-averaged flame for the 3/4 wave mode at the point of maximum heat release rate (**a**) and the point of minimum heat release rate (**b**) at φ=0.80 at Re=19000 and T_{in}=300 K.

near the expansion, inducing strong recirculation, and creating a strong shear layer between the annular jet and inner recirculation zone. The flame anchors in the shear layer between both the jet and both recirculation zones, and between the jet and the wall (Fig. 3-12(a)).

2. As the heat release falls, and the pressure rises to its maximum, the vortex is convected downstream and replaced core flow becomes columnar. The flame is unable to anchor in the core in the absence of a recirculation zone, and persists in the shear layer between the jet and the outer recirculation zone (Fig. 3-12(b) and Fig. 3-12(c))

3. The vortex continues to be convected downstream. As this happens, it shrinks in diameter and the jet reaches maximum strength. The flame remains anchored in the outer recirculation zone (Fig. 3-12(d) and Fig. 3-13(a)).

4. A new vortex forms at the expansion, and the inner recirculation zone is re-formed. The flame anchors between the newly formed inner recirculation zone and the jet, but only a small pocket of burning reactants remains in the outer recirculation zone (Fig. 3-13(b) and Fig. 3-13(c)).

5. The inner recirculation zone is fully established, and the reaction in outer re-

circulation zone intensifies, indicating fresh reactants being carried into it (Fig. 3-13(d)).

This sequence of flame images and PIV data shows a complicated series of interactions between the flow and the flame during one cycle of the 3/4 wave mode. Flame-vortex interactions near the combustor wall appear to lead to the introduction of combustion products into the outer recirculation zone, allowing a flame to establish itself between the outer recirculation zone and the jet. Fluctuations in the jet's structure are governed by the periodic vortex shedding, which sees the inner recirculation zone completely collapse and reform each cycle.

Unlike the 1/4 wave mode, we observe that the pressure oscillations lead the velocity fluctuations. The phase shift is approximately 75°, which is slightly less than the expected 90° phase shift. As with the 1/4 wave mode, the heat release is seen to lead the pressure oscillations by 70°, which is not accounted for by the acoustics model, but does satisfy the Rayleigh criterion.

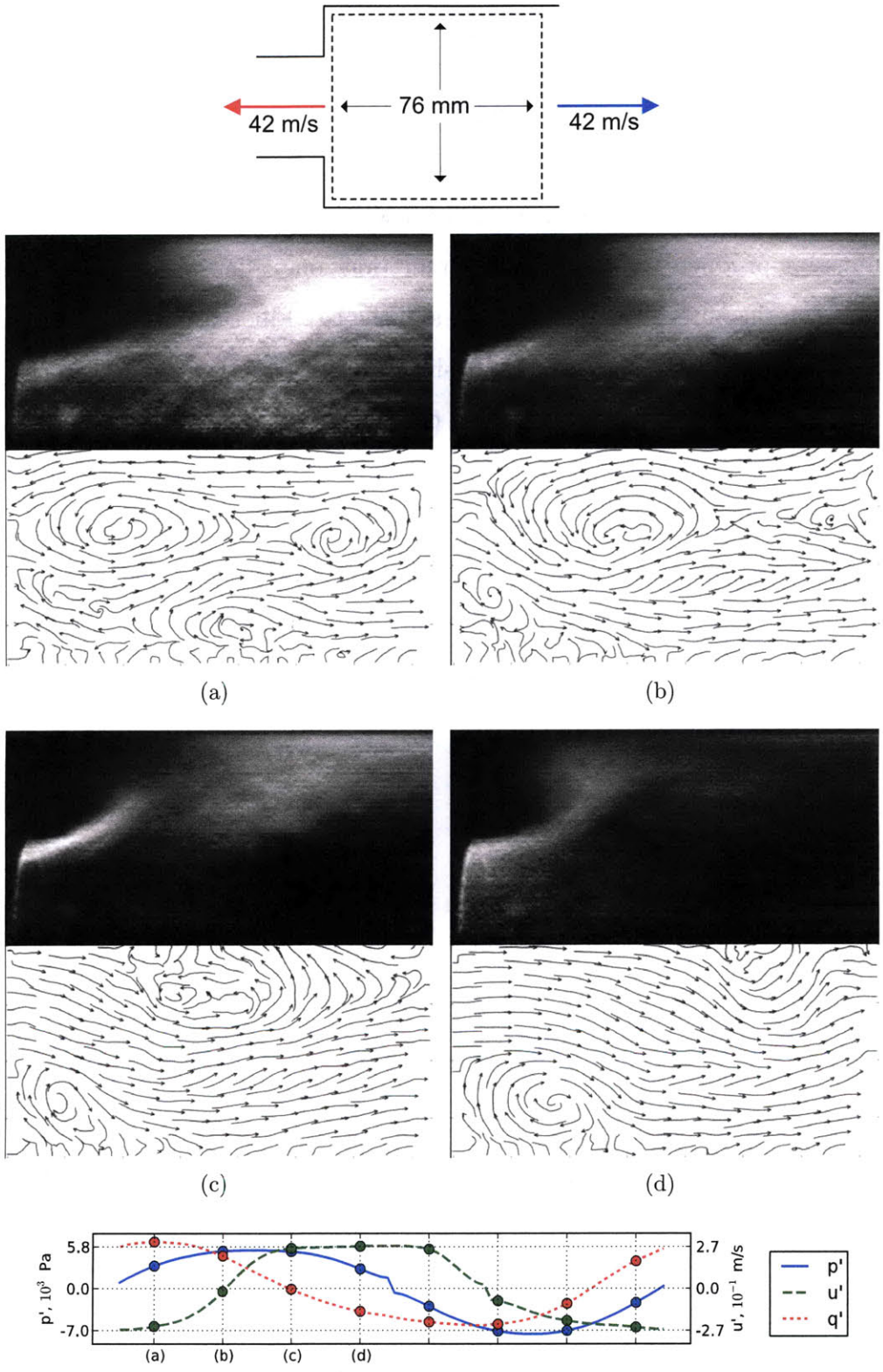

Figure 3-12: Flame images (**top**) and streamlines (**bottom**) for the 3/4 wave instability (first half of cycle). Measurements taken at Re=19000, T_{in}=300 K and φ=0.75.

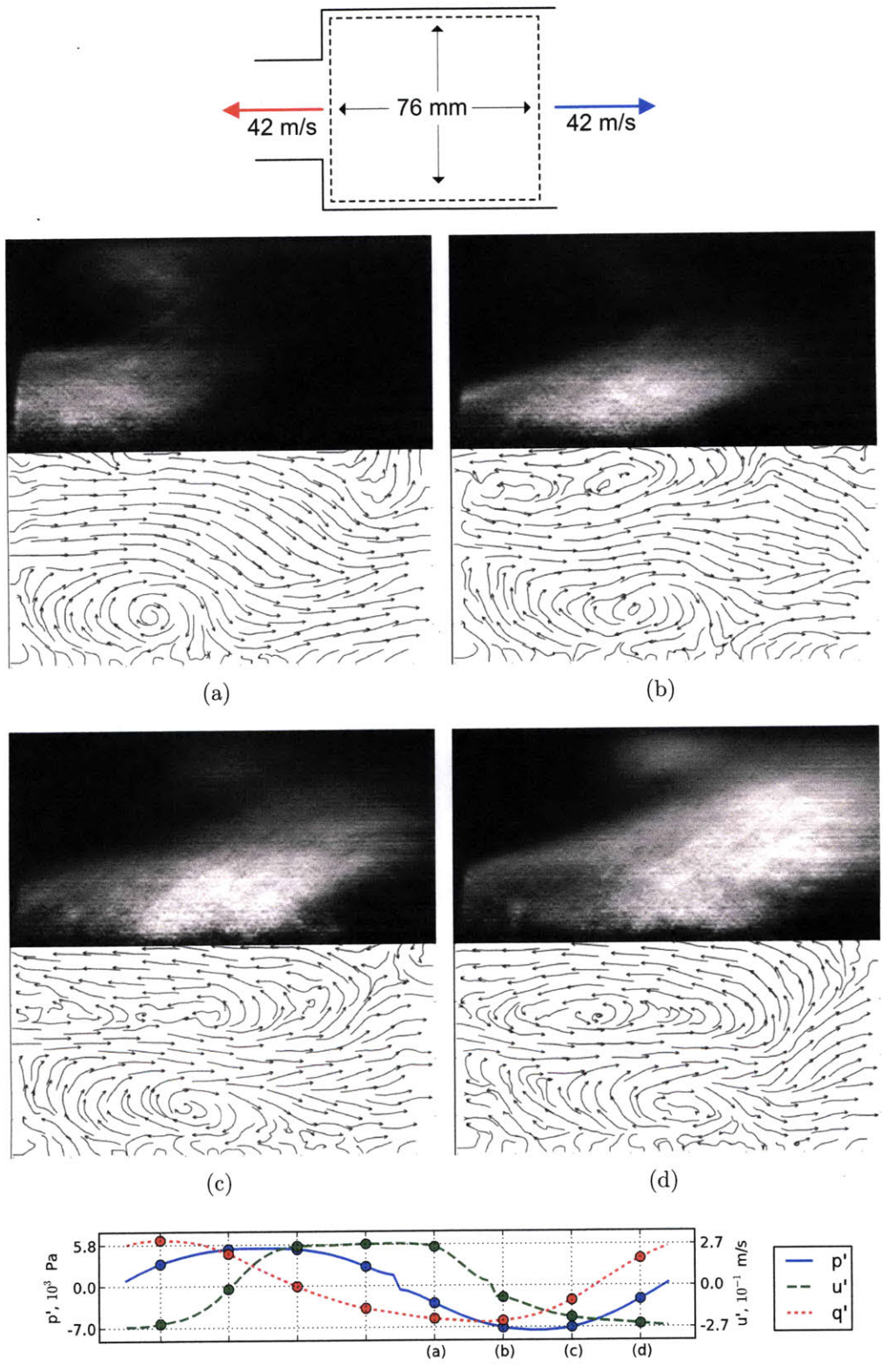

Figure 3-13: Flame images (**top**) and streamlines (**bottom**) for the 3/4 wave instability (second half of cycle). Measurements taken at Re=19000, T_{in}=300 K and φ=0.75.

Chapter 4

Microjet Modified Dynamics

The combustion instabilities decribed in Chapter 3 are representative of those that have presented a major challenge for commercial gas turbines. Previous work done in the Reacting Gas Dynamics Laboratory has shown that secondary air injection through small ports located near the flame-anchoring zone, known as *microjets*, can be effective in suppressing combustion instabilities in a backward-facing step combustor [31, 32, 33, 34]. Small-diameter ports allow for the injection of high momentum flow rates for low mass flow rates. The nearly two-dimensional geometry of the step combustor suggested two microjet configurations: normal to the flow and parallel to the flow. The geometry of the swirl combustor suggests analogous configurations: a *radial* configuration, normal to the mean flow direction and a *axial* configuration, parallel to the mean flow direction.

This work explored the application of microjets in the swirl combustor for suppressing combustion instabilities. Variants of the radial and axial microjet configurations mentioned above were tested.

The rest of this chapter discusses the design and testing of the microjets in the swirl combustor. In §4.1, the design and design methodology for the microjet injectors are discussed; in §4.2, the global effect of the various microjet configurations on the overall sound pressure level is investigated; §4.3 and discusses the behavior of the flow field at equivalence ratios where the microjets are successful at mitigating combustion instability.

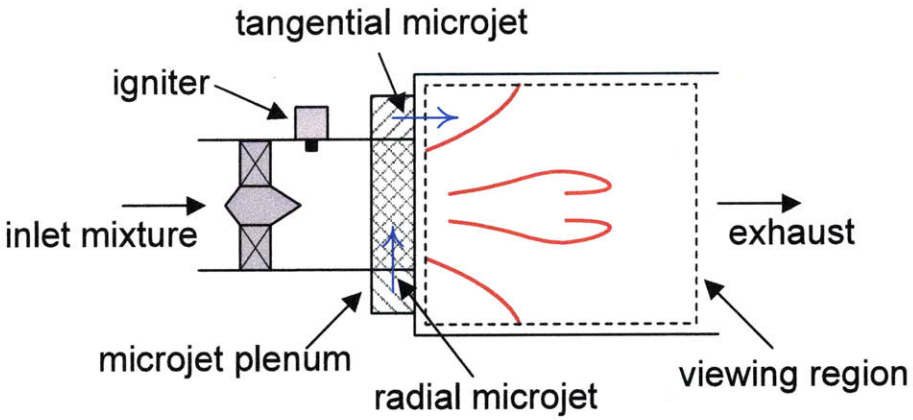

Figure 4-1: Flame anchoring region of the swirl combustor. Microjet injectors are located at or immediately upstream of the sudden expansion.

4.1 Microjet Injector Design

Microjets are small injection ports located in the flame-achoring zone of the combustor as shown in Fig. 4.1. The diameter of the ports is kept small in order to allow for high momemtum injection for low mass flow rates. For manufacturing considerations, the diameter of the microjet ports was d_{mj}=500 μm. Microjet injector blocks consist of 24 injector ports spaced 15° apart.

Microjet configurations were grouped into several different classes based on the location and direction of air injection. These different configurations are shown in Fig. 4-2. The three variables that have been studied are injection location, swirl sense and swirl angle. Microjet location is denoted as either *radial* or *axial*, with the two configuration injecting flow into the inner recirculation zone and outer recirculation zone, respectively.

Radial microjets are located immediately upstream of the sudden expansion and inject flow perpendicular to the mean velocity. Axial microjets are located at the sudden expansion at the mean diameter between the inlet and the combustion chamber. Swirl sense is either *straight* in which the flow is either directly radial or directly axial, *co-swirling* in which the injector ports are angled to inject swirl in the same sense as the main swirler, and *counter-swirling* in which the injector ports are angled so as to impart swirl in the direction opposite to the main swirler. Swirl angle is

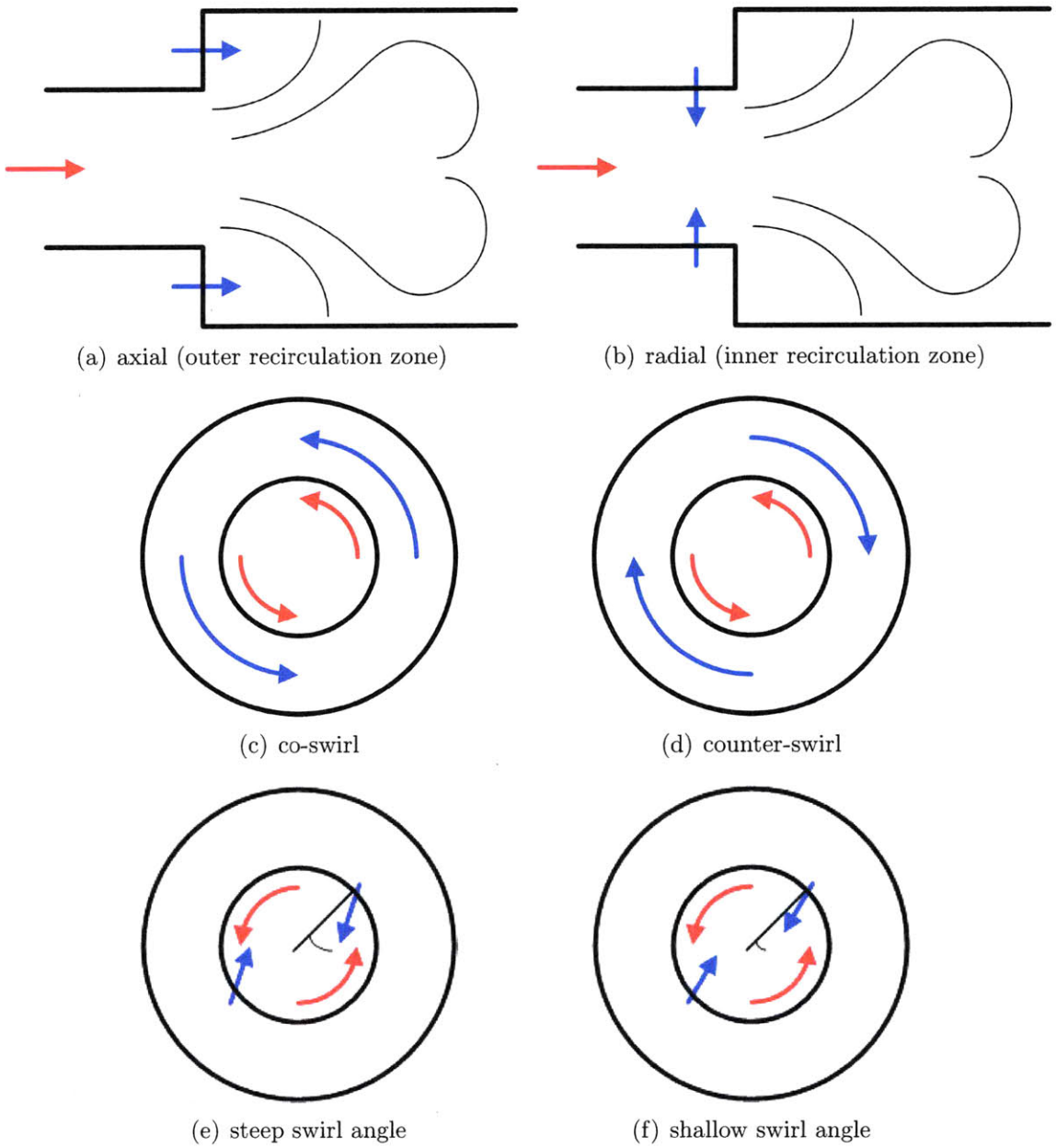

(a) axial (outer recirculation zone)

(b) radial (inner recirculation zone)

(c) co-swirl

(d) counter-swirl

(e) steep swirl angle

(f) shallow swirl angle

Figure 4-2: Geometric parameters of the microjet injectors: injector direction (location) (**a-b**), sense of swirl (**c-d**), and swirl angle (**e-f**). Main flow is red; microjet flow is blue.

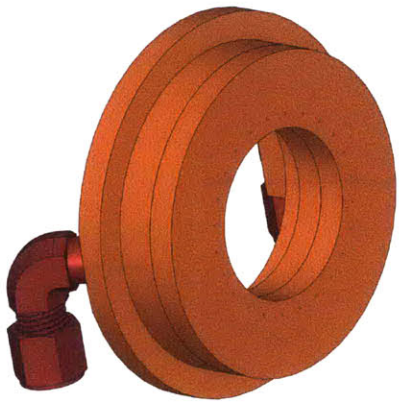

Figure 4-3: Model of axial microjet injector assembly.

measured as the angle between the port of a co-swirling or counter-swirling microjet injector and the corresponding port in a straight injector. As will be shown in §4.2, only the counter-swirling radial branch of microjets proved to be effective, and variants of these microjets were made at three different swirl angles: 20°, 35°, and 50°. A cutaway view drawing of co-swirling radial microjets along with a solid model of the injector assembly is shown in Fig. 4.1

Initial straight radial and straight axial microjet injectors were built in analogy with the normal and streamwise microjet injectors developed for the Reacting Gas Dynamics Labroatory's step combustor [33]. Subsequently, co-swirling and counter-swirling microjet injectors with 35° swirl angles were built. The injection angle was chosen such that the ratio of axial flux of tangetial momentum to the axial flux of axial momentum through the swirling axial injectors was approximately the same as through the main swirler. There is no exact analog for radial injectors, so the same offset angle was used. Counter-swirling radial microjets were shown to be effective at suppressing combustion instability for certain operating regimes, and 20° and 50° swirlers were built to study the effect of injection angle.

4.2 Acoustic Response to Microjet Injection

This section examines the acoustic modes and overall sound pressure level of the combustor while actuating the microjet injectors, which are described in §4.1. All ex-

periments were conducted at Re=19000, T_{inlet}=300 K, and with a secondary mass flow rate of $\dot{m}_{mj}$=1.6 g/s through the microjets. Microjets were operated at $\dot{m}_{mj}$=1.6 g/s. This corresponds to approximately 15% of the total mass flow when the microjets are operated. This flow rate yielded interesting dynamics. Initial exploration of the effect of mass flow rate showed no clear trend, and a full, systematic exploration of the the effect of mass flow rate has not yet been conducted; instead, other parameters were considered.

4.2.1 Axial Microjets

The first set of tests in Fig. 4-4 shows results from tests conducted using axial microjets. These microjets inject both mass and axial momentum into the combustion chamber at the sudden expansion. The overall sound pressure level shows a minimal suppression of sound amplitude when compared to the baseline case. For equivalence ratios in the range 0.57< φ <0.70, the overall sound pressure level remains within 2 dB of the 167 dB baseline instability amplitude. Both co-swirling and counter-swirling microjets result in a *higher* amplitude at the upper end of this equivalence ratio range.

All three microjets show a sharp decrease in noise amplitude at low equivalence ratios. The equivalence ratio of this dropoff is at φ=0.57 for the straight axial microjets and between φ=0.55 and φ=0.56 for both co-swirling and counter-swirling microjets. Overall sound pressure level curves for co-swirling and counter-swirling injectors closely follow each other in the region of the initial dropoff. Following the dropoff, around φ=0.53, the counter-swirling microjets excited another acoustic mode, and the overall sound pressure level curve is seen to level off and rise to 157 dB before dropping below 145 dB.

The sound pressure level spectra shown in Fig. 4-4 reveal varying dynamics for each of the microjet injectors. The dropoff at φ=0.57 for the straight axial microjets and φ=0.55 for the swirling microjets corresponds to a transition from the 3/4 wave mode to a stable mode as the equivalence ratio is decreased. Since the mass flow rate through the injectors is held constant for each run, but the two swirling microjets

are each angled 35°, albeit in opposite directions, the axial flux of axial momentum through both swirling microjets is only 67% of that through the straight microjets. This suggests that the dropoff from the 3/4 wave mode is governed by the longitudinal acoustics, not the swirl.

The mode excited at φ=0.53 for counter-swirling axial microjets is the 40 Hz one-quarter wave mode. Although a small 40 Hz component is observed for the co-swirling microjet, the overall sound pressure level is 9 dB weaker. The longitudinal acoustic boundary conditions are the same for both cases, so this effect must be a result of the interaction between swirl/co-swirl and swirl/counter-swirl.

4.2.2 Radial Microjets

The second set of results, shown in Fig. 4-5, shows data for co-swirling, straight, and counter-swirling radial microjets. The overall sound pressure level shows a very different trend than previously observed. At the upper limit, near φ=0.70, the presence of a strong 160 Hz component in the co-swirling and straight axial cases raises the sound pressure level by 2 dB and 3 dB, respectively. For the counter-swirling radial microjets, there is no 160 Hz component at φ=0.70, and the sound pressure level is 167 dB with a dominant frequency of 105 Hz, and then rises to 171 dB at φ=0.65. The sound drops from 170 dB to 147 dB between φ=0.63 φ=0.62, with no dominant oscillation. This region is considered stable. Counter-swirling radial microjets show the greatest reduction in overall sound pressure ratio over the largest operating range of the combustor.

Unlike the axial microjets, the the boundary conditions for the longitudinal acoustics are the same for all three radial microjets. Mass is added to the flow, but no additional axial momentum is added. The only effect differentiating these three cases is the sense of swirl. Compared to the baseline case in Fig. 3-2, all three cases show a significant reduction in the amplitude of the 1/4 wave mode of at least 5 dB for the two swirling microjets and 10 dB for the straight radial microjet. Aside from slight shifts in amplitude, neither the co-swirling nor the straight axial microjets altered the domain of the 3/4 mode. The 3/4 wave mode is still active down to an equivalence

ratio of φ=0.59 for these two cases, which is the same lower bound for the baseline case. The radial counter-swirling microjets raise the lower limit of the 3/4 wave mode to φ=0.63 and creates a region of stable operation between the 110 Hz and 1/4 wave modes.

4.2.3 Counter-Swirling Radial Microjets

The final dataset comparing different microjet injector design, shown in Fig. 4-6, investigates the effect of the injection angle for counter-swirling radial microjets. Microjets with injection angles of 20°, 35°, and 50° are compared to the baseline acoustics of the combustor.

All three microjet injectors increase lower equivalence ratio limit of the 3/4. The lower limit is increases from φ=0.59 in the baseline case to φ=0.63 for the 20° and 35° injectors. The 50° injector raises the lower limit of the 3/4 wave mode to φ=0.61.

4.2.4 Counter-Swirling Radial Microjets for in Syngas

The effect of 20° counter-swirling microjets is on various syngas compositions is shown in Fig. 4-7, Fig. 4-8, Fig. 4-9, and Fig. 4-10. From the perspective of suppressing combustion instability, these results are significantly less promising than the tests conducted with propane/air flames. In each case studied, the microjets decereased the stable operating range of the combustor.

In each case, the microjets either increased the equivalence ratio range and amplitude of the one-quarter wave (40 Hz) mode, or excited that mode even though it was not present in the baseline case at all. This lends further credence to the observations mentioned previously that the one-quarter wave mode is strongly affected by the swirl of the flow.

4.2.5 Summary of Microjet Results

In the preceeding section, acoustic analyses were shown for eight different microjet configurations. Axial microjets proved to reduce the lower operating limit of the 110

Hz instability, increasing the range of instability, which is an undesirable result from the perspective of combustor and control system design. Radial microjet configurations reduced the amplitude of the 40 Hz mode, without decreasing the lower limit of the 110 Hz mode. Furthermore, counter-swirling radial microjets both reduced the amplitude of the 40 Hz mode and increased the minimum equivalence ratio of the 110 Hz mode, opening a stable window of operation between the two modes. This configuration is the most promising for application in combustor design.

These results are summarized in Table 4.1.

Configuration	Effect
Radial counter-swirling 50°	Peak reduction of 40 Hz mode by 17 dB
	Increase of ϕ_{min} of 110 Hz mode to 0.61
Radial counter-swirling 35°	Peak reduction of 40 Hz mode by 5 dB
	Increase of ϕ_{min} of 110 Hz mode to 0.63
Radial counter-swirling 20°	Peak reduction of 40 Hz mode by 11 dB
	Increase of ϕ_{min} of 110 Hz mode to 0.63
Radial straight	Peak reduction of 40 Hz mode by 21 dB
Radial co-swirling 35°	Peak reduction of 40 Hz mode by 16 dB
Axial counter-swirling 35°	Decrease of ϕ_{min} of 110 Hz mode to 0.55
Axial straight	Decrease of ϕ_{min} of 110 Hz mode to 0.57
Axial co-swirling 35°	Decrease of ϕ_{min} of 110 Hz mode to 0.55

Table 4.1: Summary of major effects of different microjet configurations for 1.6 g/s mass flow rate (15% of total mass flow), at Re=19 000 and T_{inlet}=300 K.

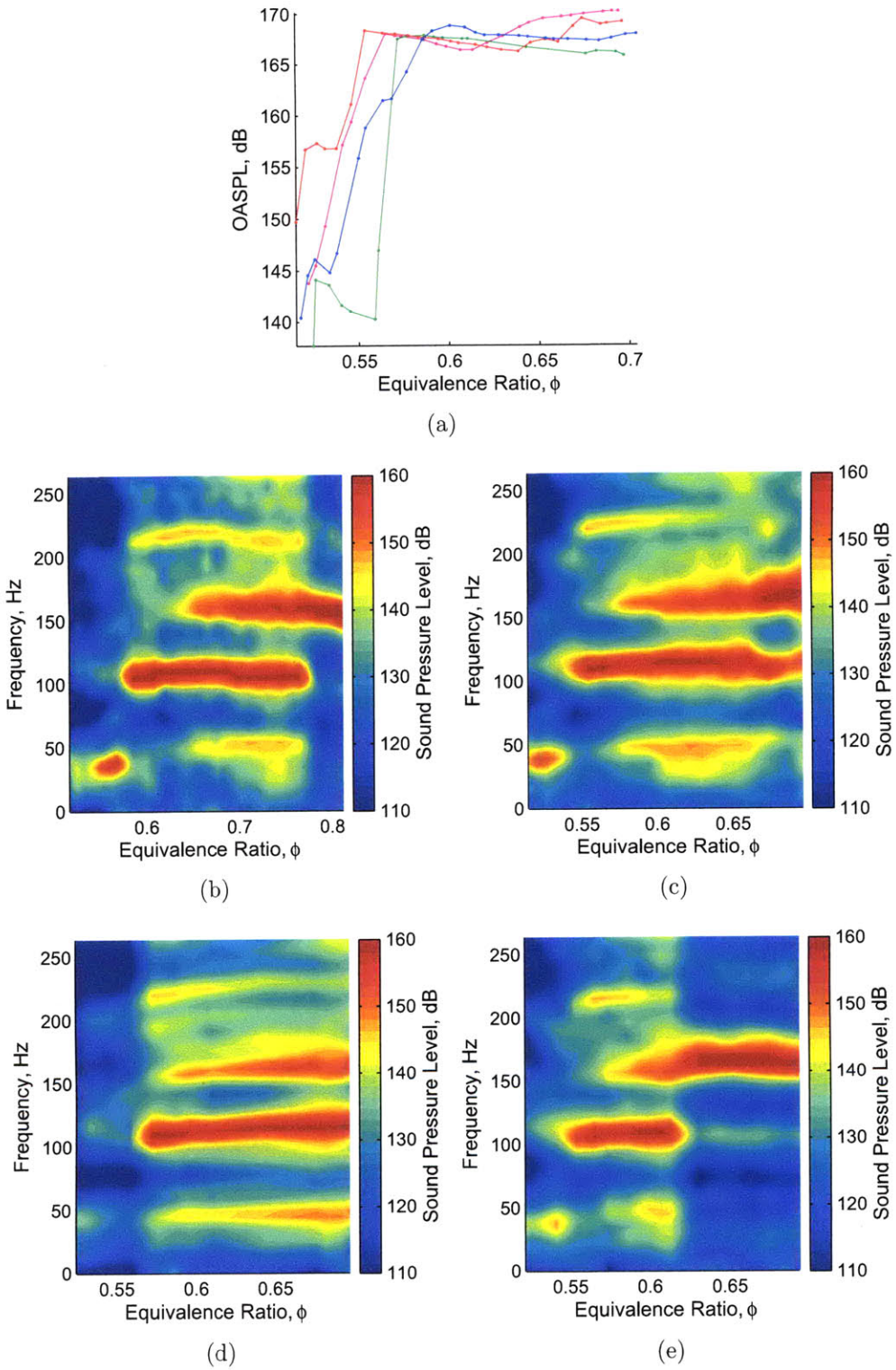

Figure 4-4: Microjet-modified acoustics demonstrating the use of axial microjets at Re=19000 and T_{inlet}=300 K for $\dot{m}_{mj}$=1.6 g/s. The OASPL plot (**a**) and sound pressure level maps showing with no microjets (**blue,b**), and axial counter-swirling microjets (**red,c**), straight microjets (**green,d**), and co-swirling microjets (**magenta,e**).

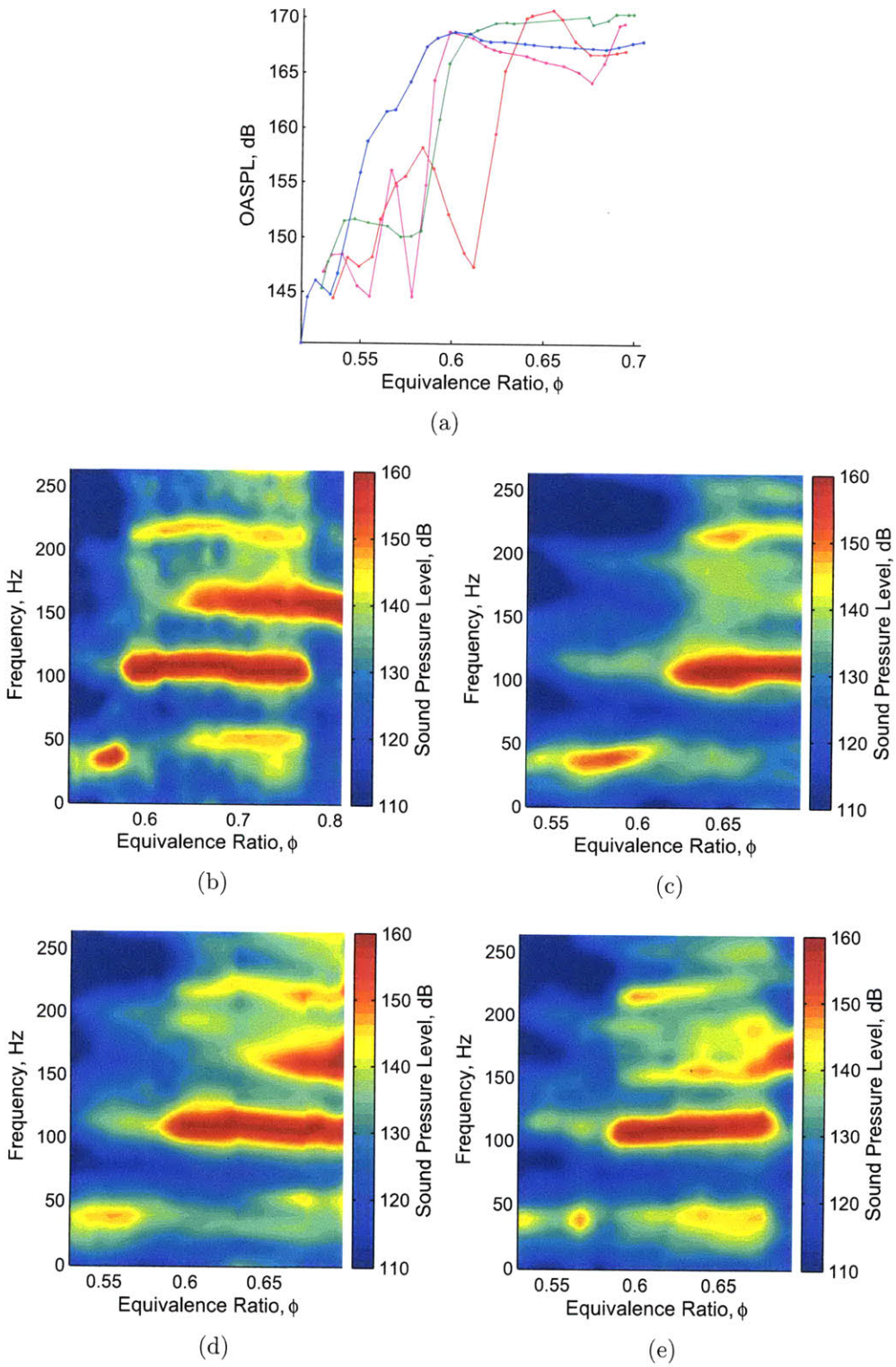

Figure 4-5: Microjet-modified acoustics demonstrating the use of radial microjets at Re=19000 and T_{inlet}=300 K for $\dot{m}_{mj}$=1.6 g/s. The OASPL plot (**a**) and sound pressure level maps showing with no microjets (**blue,b**), and radial counter-swirling microjets (**red,c**), straight microjets (**green,d**), and co-swirling microjets (**magenta,e**).

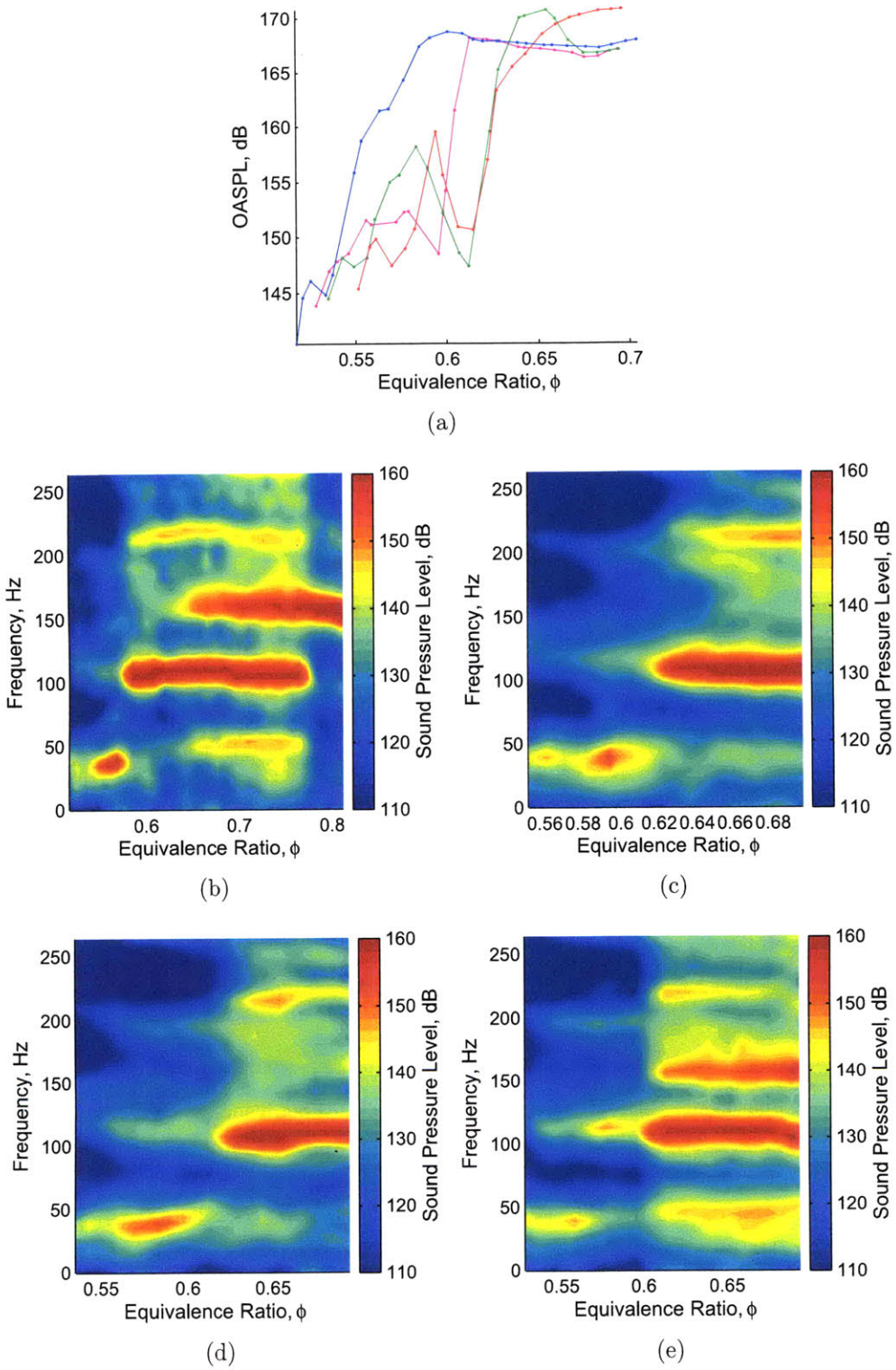

Figure 4-6: Microjet-modified acoustics demonstrating the use of counter-swirling radial microjets at Re=19000 and T_{inlet}=300 K for $\dot{m}_{mj}$=1.6 g/s. The OASPL plot (**a**) and sound pressure level maps showing with no microjets (**blue,b**), and counter-swirling radial microjets at 20° (**red,c**), 35° (**green,d**), and 50° (**magenta,e**).

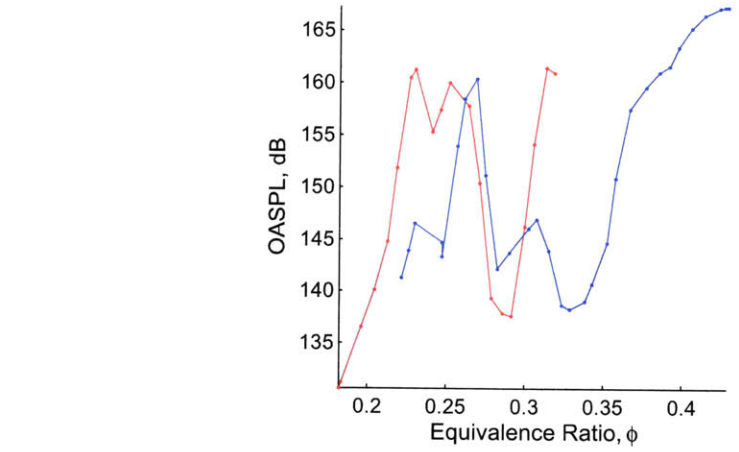

(a)

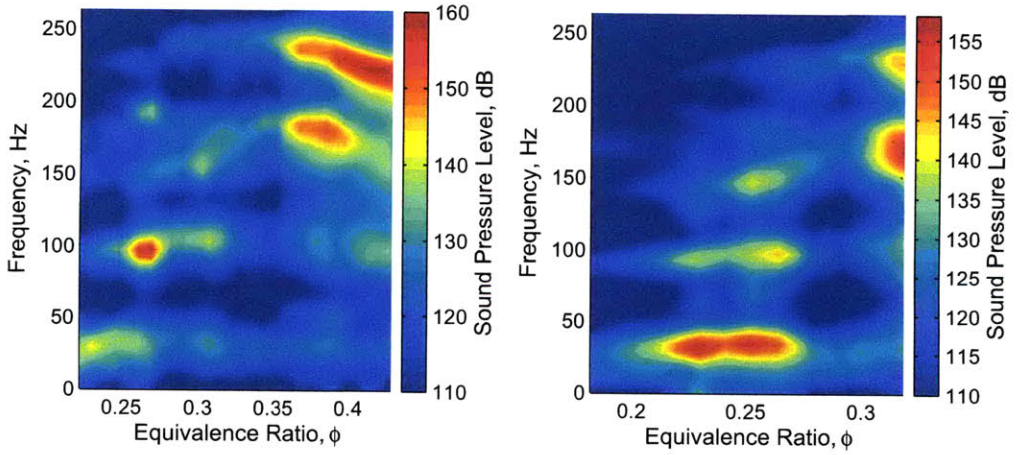

(b) (c)

Figure 4-7: Acoustics for syngas (20% CO, 80% H_2) at Re=19000 and T_{in}=300 K. Plot of OASPL (**a**) with no microjets (**blue**) and with 1.6 g/s of microjet air injection (**red**). Sound pressure level map without microjets (**b**) and with microjets (**c**).

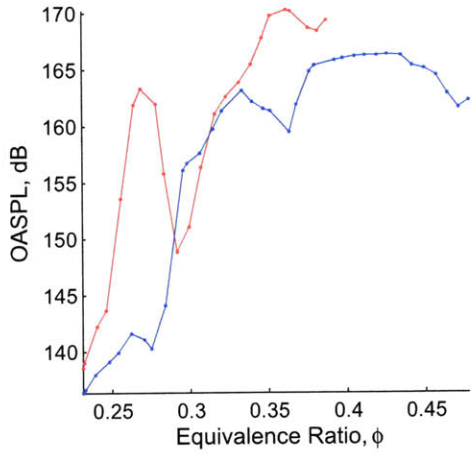

(a)

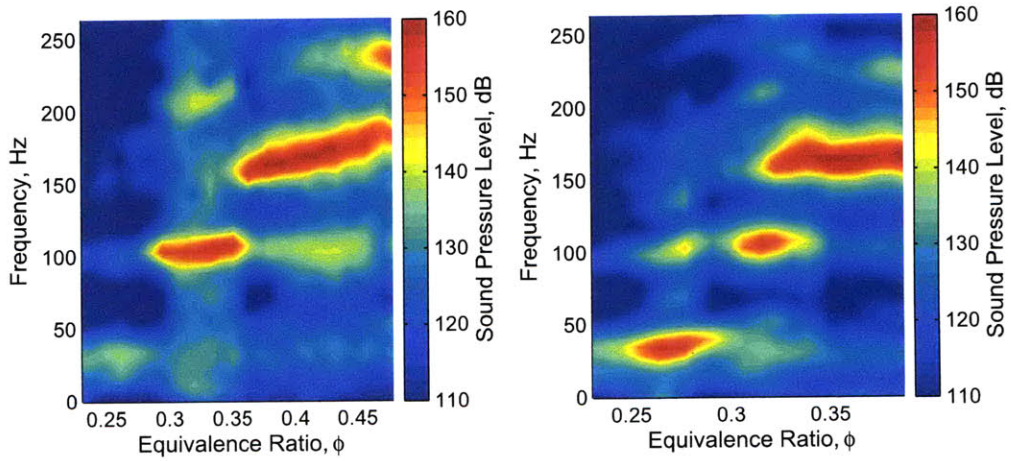

(b) (c)

Figure 4-8: Acoustics for syngas (40% CO, 60% H_2) at Re=19000 and T_{in}=300 K. Plot of OASPL (**a**) with no microjets (**blue**) and with 1.6 g/s of microjet air injection (**red**). Sound pressure level map without microjets (**b**) and with microjets (**c**).

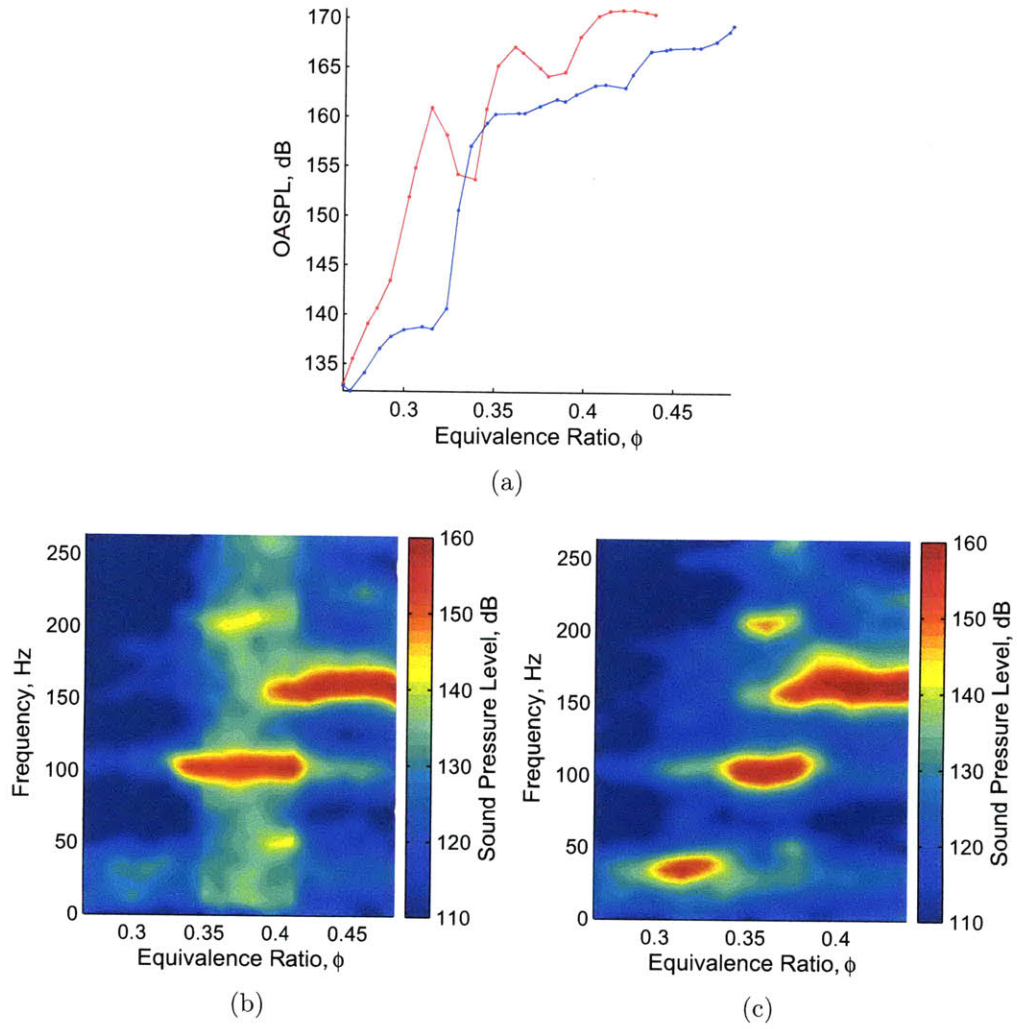

Figure 4-9: Acoustics for syngas (60% CO, 40% H_2) at Re=19000 and T_{in}=300 K. Plot of OASPL (**a**) with no microjets (**blue**) and with 1.6 g/s of microjet air injection (**red**). Sound pressure level map without microjets (**b**) and with microjets (**c**).

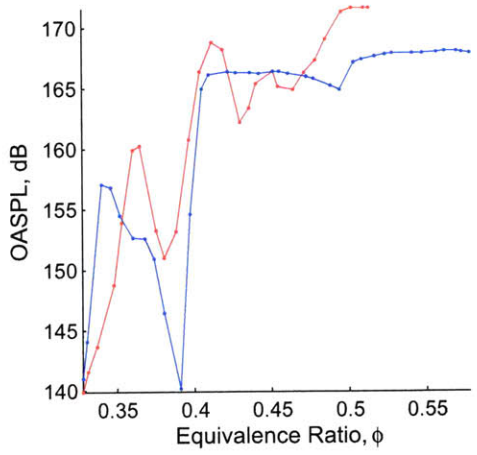

(a)

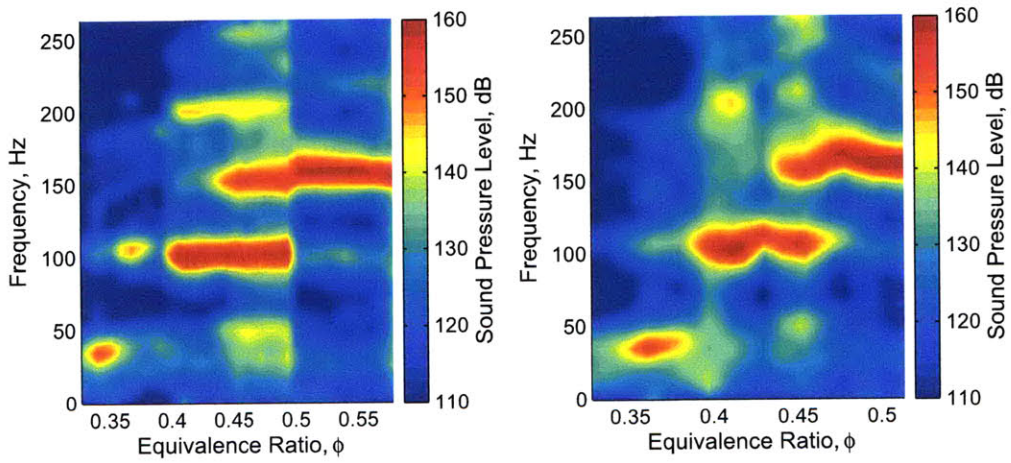

(b) (c)

Figure 4-10: Acoustics for syngas (80% CO, 20% H_2) at Re=19000 and T_{in}=300 K. Plot of OASPL (**a**) with no microjets (**blue**) and with 1.6 g/s of microjet air injection (**red**). Sound pressure level map without microjets (**b**) and with microjets (**c**).

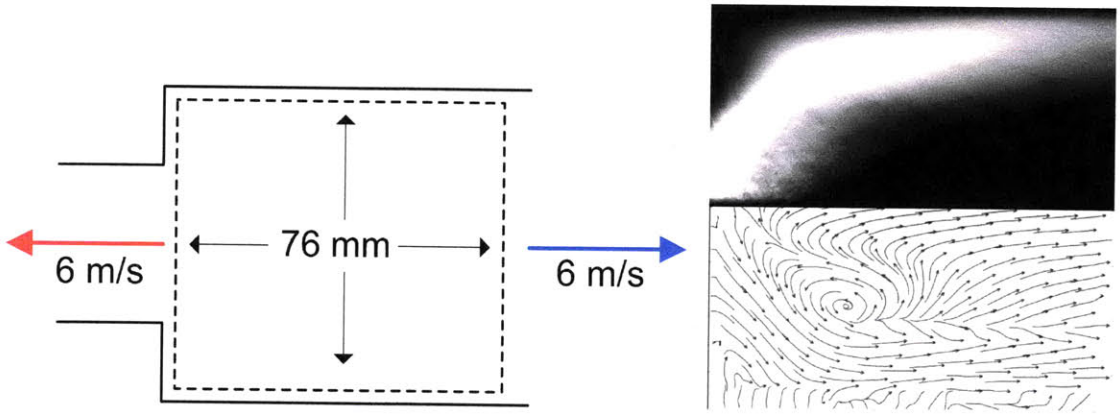

Figure 4-11: Average stable flame image (**top**) and streamlines (**bottom**) for the microjet stabilized flame at φ=0.6, Re=19000, T_{in}=300 K for 35° counter-swirling radial microjets with $\dot{m}_{mj}$=1.6 g/s of secondary air flow (corresponding to 15% of the total mass flow).

4.3 Stabilized Flame

The microjet configuration of the greatest interest is the radial counter-swirling injector operating under conditions where it suppresses combustion instability. Flame images and PIV data are presented at φ=0.6, Re=1900, and T_{in}=300 K for the case where 1.6 g/s of air is injected through the 35° radial counter-swirling microjets. The reported equivalence ratio accounts for the dilution effect of the secondary air injection by computing

$$\phi = \frac{\dot{m}_{fuel}/(\dot{m}_{inlet} + \dot{m}_{mj})}{(\dot{m}_{fuel}/\dot{m}_a ir)_{stoich}} \tag{4.1}$$

where $\dot{m}_{inlet}$ is the main air mass flow rate and $\dot{m}_{mj}$ is the mass flow rate through the microjets.

The flame and flow field, shown in Fig. 4-11, are qualitatively very different from any of the cases with no microjet air injection. Notably, the vortex breakdown takes the form of four-cell bubble, as discusses in §1.2, which is characteristic of flows with high swirl numbers. Combustion products are recirculated back into the reactants via a toroidal vortex, but a second, counter-rotating toroidal vortex also carries some of these products back out of the recirculation bubble and allows them to convect downstream. The flame is anchored on the upstream edge of the inner recirculation

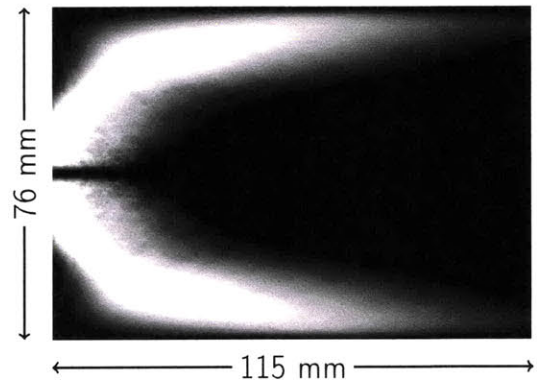

Figure 4-12: Average microjet stabilized flame at φ=0.60, Re=19000, and T_{in}=300 K with $\dot{m}_{mj}$=1.6 g/s of secondary air flow (15% of the total mass flow).

zone. The greatest intensity is in the conical region of the flame (see Fig. 4-12), in contrast with the lean stable flame (see Fig. 3-5). The flame does not extend far beyond the point at which the jet impinges on the combustor wall. Comparing this flame to the baseline stable flame, we see that the stabilized flame is significantly more compact, with an estimated length of ℓ_f=115 mm, compared to the ℓ_f=220 mm of the lean stable flame. A flame such as this is more desirable for practical applications.

One of the most notable features of this case is the swirl pattern. As previsouly shown, both stable and unstable cases yielded very similar normalized swirl patterns for both stable and unstable cases. Swirl velocity at a given radius shows little variation along the axis and in time. In Fig. 4-13, the swirl velocity for the stable and microjet stabilized cases are shown. The absolute swirl velocities are shown in Fig. 4-13(a), and Fig. 4-13(b) shows the swirl velocity normalized by the mean magnitude of the velocity. The sense of swirl has been completely reversed by the microjets; that is, the flow swirls in the direction opposite of the main swirler. Additionally, the magnitude of the swirl velocity is higher, particularly in the core of the longitudinal vortex. Downstream of the flame, the fluid density is approximately constant, and the swirl number can be computed. The swirl number for the microjet stabilized flow is computed as S=1.0, compared to S=0.53 for the lean stable flame.

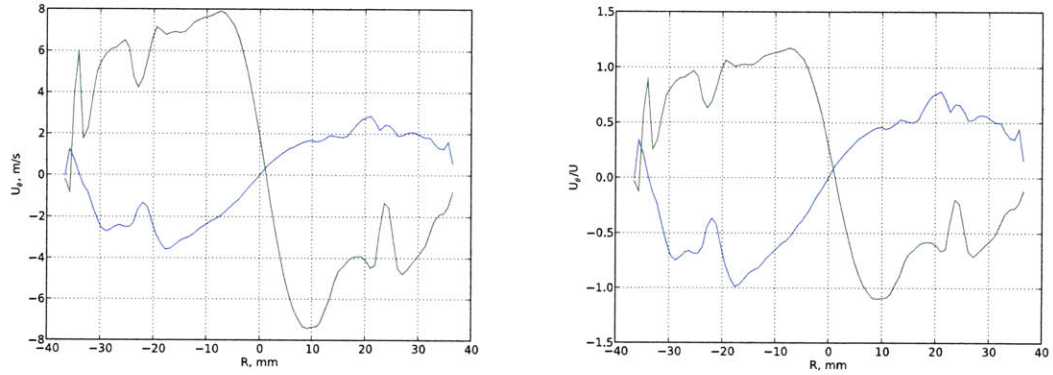

(a) (b)

Figure 4-13: Absolute (**a**) and normalized (**b**) swirl velocity averaged along the combustor axis for the microjet stabilized flame (**green**) at φ=0.6, Re=19000, T_{in}=300 K for 35° counter-swirling radial microjets with $\dot{m}_{mj}$=1.6 g/s of secondary air flow and the stable flame (**blue**) at φ=0.70.

Chapter 5

Conclusion

The overarching goal of this thesis and the Combustion Dynamics Group in the Reacting Gas Dynamics Laboratory is to develop a physical understanding of the mechanism or mechanisms that lead to combustion instability in order to greatly improve the design process for low-NO_x lean-premixed combustors. The contributions of this thesis have been

1. to develop and implement procedures necessary to use high-speed stereoscopic PIV for probing axisymmetric, reacting flow;

2. to design and test microjet injectors for passive suppression of combustion instability; and

3. to investigate the mechanisms that are responsible for combustion instability in swirling, axisymmetric flows through the use of flow injection and optical diagnostic techniques.

Experimental trials with the PIV system resulted in the development of a set of guidelines for dealing with the challenges inherent in working with reacting, confined flows. In particular, mitigating internal reflections and preventing particle accumulation on the combustion chamber walls proved to be the largest challenges. Fine-grained sandblasting of the inner walls of the combustion chamber, in areas that were not required to be optically accessible, proved to reduce the level of internal reflections sufficiently that PIV could be applied. Electrostatic forces were determined to

be a major contributor to the accumulation of seeding particles on the inner wall of the combustor. This problem was solved through periodic cleaning of the tube with anti-static cloth and careful handling with anti-static gloves.

The flowfield inside the combustion chamber is dominated by two vortical structures: the outer recirculation zone, and the inner recirculation zone. These expected structures were experimentally verified through the use of PIV. Microjets were developed around two strategies: modification of the outer recirculation zone dynamics and modification of the inner recirculation zone dynamics. Outer recirculation zone modification was achieved through the injection of secondary air at the sudden expansion in the axial direction; inner recirculation zone modification was achieved through radial injection of secondary air immediately upstream of the sudden expansion. The swirling nature of the flow suggested three configurations for each type of injector: counter-swirling, co-swirling, and straight (not swirling). Additionally, after determining that only the counter-swirling radial microjets showed significant reduction in the overall sound pressure level inside the combustor, three different injection angles for this configuration were tested: 20°, 35°, and 50°.

Particular attention was paid to the dynamics of the combustor at lean equivalence ratios, just above the lean blowoff limit. Two modes of instability dominate this operating regime: the 40 Hz one-quarter wave mode, and the 105 Hz three-quarter wave mode. In the baseline dynamics of the combustor, the 1/4 wave mode is dominant for a narrow band of equivalence ratios ($0.55 \leq \varphi \leq 0.58$), and reaches a sound pressure level of 165 dB in this region at this frequency. An incremental increase in the equivalence ratio results in a transition from the 1/4 wave mode to the 3/4 wave mode, which reaches a sound pressure level of 168 dB as the equivalence ratio increases up to φ=0.82.

Modification of the outer recirculation zone through the use of axial microjets seems fails to substantially increase the stable operating range of the combustor. Transition to the 3/4 wave mode is seen to happen at a higher equivalence ratio for both counter-swirling and co-swirling axial microjets than for straight axial microjets, strongly suggesting that the transition is due an interaction between the heat release

in the flame and the axial momentum injection modifying the acoustic boundary conditions rather than an effect due to modification of the flow field in the outer recirculation zone. The amplitude of the 1/4 wave mode is significantly reduced only in the case of the counter-swirling axial microjets. Neither co-swirling nor straight radial microjets significantly reduced the amplitude of the 40 Hz mode, suggesting that swirl dynamics, rather than modification of the acoustic boundary conditions is responsible for this mode.

Radial microjets reduced the amplitude of the 1/4 wave mode and an increased lower equivalence ratio limit of the 3/4 wave mode. The co-swirling and straight radial microjets both raised the lower bound for the 3/4 wave mode to φ=0.58, while the counter-rotating radial microjets increased the lower limit to φ=0.62. This suggests two mechanisms for increasing this lower limit: modification of the acoustic boundary conditions through mass injection (no axial momentum was injected through radial microjets), and stabilization through the modification of the inner recirculation zone. As with the axial microjets, the counter-swirling radial microjets exhibited a much stronger 1/4 wave mode than either the co-swirling or straight radial microjets, again suggesting that the 1/4 wave mode is strongly effected by the swirl of the flow.

Coupled with the noted differences in their response to microjet air injection, the 1/4 wave and 3/4 wave modes show qualitatively very different flow dynamics. The 3/4 wave instability is extremely active, with time-varying flame location and periodic collapse of the vortex breakdown bubble corresponding to unsteady vortex shedding. The 1/4 wave mode, in contrast, displays a stationary flame, despite strong acoustic oscillations. Unlike the 3/4 wave mode, which has no fixed annular vortices in the inside of the jet, the 1/4 wave mode features a fixed annular vortex that creates the inner recirculation zone. Counter-rotating vortices are shed from the expansion, and interact with the fixed vortex in such a way that the recirculation weakens significantly and a weak core jet forms for part of the cycle.

From the perspective of development of instability suppression technologies, the counter-swirling radial microjets have shown a good deal of promise. For both propane/air and high-CO syngas/air flames, they yield an increased lower equiva-

lence ratio limit for the 3/4 wave mode as well as a reduced amplitude of the 1/4 wave mode. The result is a stable operating regime, with no dominant acoustic frequency, at equivalence ratios slightly above the blowoff limit. Notably, the flame that forms on the leading edge of the inner recirculation zone for the microjet-stabilized case is also more compact than the stable flame observed at low equivalence ratios near the lean blowoff limit.

5.1 Recommendations for Future Work

The research presented in this thesis, while introducing some new insight into the mechanics of thermoacoustic instability, has opened up several questions for exploration. In particular, there appears to be two mechanisms of instability at work in the 40 Hz and 110 Hz modes for propane/air flames (and also seen in syngas/air flames). The first appears to be coupled to the swirl. Without modifying the acoustic boundary conditions of the system, the injection of swirling secondary air (particularly counter-swirling seconday air) has been shown to excite or amplify the one-quarter wave mode of the combustor, but little change is seen to the structure of the flame or flow field. The second mechanism is the periodic vortex breakdown that is seen in the 110 Hz mode for propane/air flame (similar flame dynamics are observed for syngas, but there is currently no PLIF data to verify the similarity). The instability couples with the vortex breakdown, leading to a very dynamic flow field.

The further characterization of these two mechanisms is the most logical next step for this research. The combustor in which this work was conducted was not initially designed for full optical accessibility. We recommend future work is conducted in such a way that upstream and downstream flow measurements can readily be made and the flame achoring can directly be observed.

Bibliography

[1] C. Brücker and W. Althaus, "Study of vortex breakdown by particle tracking velocimetry (ptv)," *Experiments in Fluids*, vol. 13, pp. 339–349, 1992.

[2] J. H. Faler and S. Leibovich, "An experimental map of the internal structure of a vortex breakdown," *Journal of Fluid Mechanics*, vol. 86, no. 2, pp. 313–335, 1978.

[3] C. M. Vest, "Formation of images from projections: Radon and abel transforms," *Journal of the Optical Society of America*, vol. 64, no. 9, pp. 1215–1218, 1974.

[4] J. M. Beér, "Combustion technology developments in power generation in response to environmental challenges," *Progress in Energy and Combustion Science*, vol. 26, pp. 301–327, 2000.

[5] J. W. Rayleigh, "The explanation of certain acoustical phenomena," *Nature*, vol. 18, pp. 319–321, July 1878.

[6] B.-T. Chu, "On the energy transfer to small disturbances in fluid flow (part i)," *Acta Mechanica*, vol. 1, no. 3, pp. 215–234, 1965.

[7] Y. Huang, S. Wang, and V. Yang, "Systematic analysis of lean-premixed swirl-stabilized combustion," *AIAA Journal*, vol. 44, no. 4, pp. 724–740, 2006.

[8] R. Weber and J. Dugué, "Combustion accelerated swirling flows in high confinements," *Progress in Energy and Combustion Science*, vol. 18, pp. 349–367, 1992.

[9] R. E. Spall, T. B. Gatski, and R. L. Ash, "The structure and dynamics of bubble-type vortex breakdown," *Proceedings of the Royal Society of London A*, vol. 429, pp. 613–637, 1990.

[10] S. Wang and Z. Rusak, "The dynamics of a swirling flow in a pipe and transition to axisymmetric vortex breakdown," *Journal of Fluid Mechanics*, vol. 340, pp. 177–223, 1997.

[11] T. B. Benjamin, "Theory of the vortex breakdown phenomenon," *Journal of Fluid Mechanics*, vol. 23, pp. 593–629, 1962.

[12] P.-H. Renard, D. Thévenin, J. C. Rolon, and S. Candel, "Dynamics of flame/vortex interactions," *Progress in Energy and Combustion Science*, vol. 26, pp. 225–282, 2000.

[13] A. M. Annaswamy and A. F. Ghoniem, "Active control of combustion instability: Theory and practice," *IEEE Control Systems Magazine*, vol. 22, 37-54 2002.

[14] N. Docquier and S. Candel, "Combustion control and sensors: A review," *Progress in Energy and Combustion Science*, vol. 28, pp. 107–150, 2002.

[15] Y. Huang and V. Yang, "Dynamics and stability of lean-premixed swirl-stabilized combustion," *Progress in Energy and Combustion Science*, vol. 35, pp. 293–364, 2009.

[16] C. O. Paschereit, E. Gutmark, and W. Weisenstein, "Structure and control of thermoacoustic instabilities in a gas-turbine combustor," *Combustion Science and Technology*, vol. 138, no. 1, pp. 213–232, 1998.

[17] G. A. Richards, D. L. Straub, and E. H. Robey, "Passive control of combustion dynamics in stationary gas turbines," *Journal of Propulsion and Power*, vol. 19, no. 5, pp. 795–810, 2003.

[18] K. S. Kedia, H. M. Altay, and A. F. Ghoniem, "Impact of flame-wall interaction on premixed flame dynamics and transfer function characteristics," *Proceedings of the Combustion Institute*, 2010.

[19] C. J. Dasch, "One-dimensional tomography: A comparison of abel, onion-peeling, and filtered backprojection methods," *Applied Optics*, vol. 31, pp. 1146–1152, March 1992.

[20] S. A. Filatyev, M. P. Thariyan, R. P. Lucht, and J. P. Gore, "Simultaneous stereo particle image velocimetry and double-pulsed planar laser-induced fluorescence of turbulent premixed flames," *Combustion and Flame*, vol. 150, pp. 201–209, 2007.

[21] B. Dam, G. Corona, and A. Choudhuri, "Investigation of flashback propensity in turbines with syngas fuels," *48th AIAA Aerospace Sciences Meeting and Exhibit*, January 2010.

[22] A. Stella, G. Guj, J. Kompenhans, M. Raffel, and H. Richard, "Application of particle image velocimetry to combusting flows: Design considerations and uncertainty assessment," *Experiments in Fluids*, vol. 30, pp. 167–180, 2001.

[23] J. Sung and J. Y. Yoo, "Three-dimensional phase averaging of time-resolved piv measurement data," *Measurement Science and Technology*, vol. 12, pp. 655–662, 2001.

[24] R. L. Speth, H. M. Altay, D. E. Hudgins, and A. F. Ghoniem, "Dynamics and stability limits of syngas combustion in a swirl-stabilized combustor," *Proceedings of ASME Turbo Expo*, June 2008.

[25] K. R. McManus, T. Poinsot, and S. M. Candel, "A review of active control of combustion instabilities," *Progress in Energy and Combustion Science*, vol. 19, pp. 1–29, 1993.

[26] M. M. A. Fleifil, *Trade-Off Between NO_x Emission and Thermoacoustic Instability: Mediation and/or Control.* PhD thesis, Ain Shams University, 1995.

[27] A. P. Dowling and S. R. Stow, "Acoustic analysis of gas turbine combustors," *Journal of Propulsion and Power*, vol. 19, pp. 751–764, September-October 2003.

[28] S. Wang and Z. Rusak, "On the stability of an axisymmetric rotating flow in a pipe," *Physics of Fluids*, vol. 8, pp. 1007–1016, April 1996.

[29] S. Wang and Z. Rusak, "On the stability of non-columnar swirling flows," *Physics of Fluids*, vol. 8, pp. 1017–1023, April 1996.

[30] Z. Rusak, A. K. Kapila, and J. J. Choi, "Effect of combustion on near-critical swirling flow," *Combustion Theory and Modeling*, vol. 6, no. 4, pp. 625–645, 2002.

[31] H. M. Altay, D. E. Hudgins, R. L. Speth, A. M. Annaswamy, and A. F. Ghoniem, "Mitigation of thermoacoustic instability utilizing steady air injection near the flame anchoring zone," *Combustion and Flame*, vol. 157, pp. 686–700, 2010.

[32] H. M. Altay, *Physics-Based Flame Dynamics Modeling and Thermoacoustic Instability Mitigation.* PhD thesis, Massachusetts Institute of Technology, 77 Massachusetts Ave., Cambridge, MA USA, 2009.

[33] D. E. Hudgins, "Suppression of premixed combustion dynamics utilizing microjet air injection," Master's thesis, Massachusetts Institute of Technology, 77 Massachusetts Ave., Cambridge, MA USA, 2008.

[34] H. M. Altay, R. L. Speth, D. Snarheim, D. E. Hudgins, A. F. Ghoniem, and A. M. Annaswamy, "Impact of microjet actuation on stability of a backward-facing step combustor," *45rd AIAA Aerospace Sciences Meeting and Exhibit*, 2007.